Constraints on the nuclear symmetry energy from asymmetric-matter calculations with chiral *NN* and 3*N* interactions

R. Somasundaram [1,*] C. Drischler [2,3,†] I. Tews [4,‡] and J. Margueron [1,§]

[1]*Univ Lyon, Univ Claude Bernard Lyon 1, CNRS/IN2P3, IP2I Lyon, UMR 5822, F-69622, Villeurbanne, France*
[2]*Department of Physics, University of California, Berkeley, California 94720, USA*
[3]*Nuclear Science Division, Lawrence Berkeley National Laboratory, Berkeley, California 94720, USA*
[4]*Theoretical Division, Los Alamos National Laboratory, Los Alamos, New Mexico 87545, USA*

The nuclear symmetry energy is a key quantity in nuclear (astro)physics. It describes the isospin dependence of the nuclear equation of state, which is commonly assumed to be almost quadratic. In this work, we confront this standard quadratic expansion of the equation of state with explicit asymmetric nuclear-matter calculations based on a set of commonly used Hamiltonians including two- and three-nucleon forces derived from chiral effective-field theory. We study, in particular, the importance of nonquadratic contributions to the symmetry energy, including the nonanalytic logarithmic term introduced by Kaiser [Phys. Rev. C **91**, 065201 (2015)]. Our results suggest that the nonquadratic contribution to the symmetry energy can be systematically determined from the various Hamiltonians employed, and we obtain $0.74^{+0.11}_{-0.08}$ MeV (or $-1.02^{+0.11}_{-0.08}$ MeV for the potential term with the effective-mass contribution) at nuclear saturation density, while the logarithmic contribution to the symmetry energy is relatively small and model-dependent. We also employ the meta-model approach to study the impact of the higher-order contributions on the neutron-star crust-core transition density, and find a 5% correction.

I. INTRODUCTION

The nuclear-matter equation of state (EOS) is of great interest for nuclear physics, see recent reviews [1–3] and references therein. It connects bulk properties of atomic nuclei, with small isospin asymmetry, with neutron-rich matter inside neutron stars (NSs) [4,5]. The isospin dependence of the nuclear-matter EOS is described by the nuclear symmetry energy which, for example, governs the proton fraction in beta-equilibrium, determines the pressure in the core of NSs, and hence, the NS mass-radius relation [6–8], or cooling via the direct URCA process [9]. Due to its importance for many physical systems, the symmetry energy and its density dependence were identified as key quantities for nuclear (astro)physics in the 2015 DOE/NSF Nuclear Science Advisory Committee Long Range Plan for Nuclear Science [10], and are actively investigated by combining information from nuclear theory, astrophysics, and experiments.

Because NS observations still come with sizable uncertainties, the symmetry energy and its density dependence cannot be inferred from NS properties alone [9]. Hence, various constraints on the symmetry energy have been inferred from experimental data, e.g., determinations of neutron skins in lead (PREX) and calcium (CREX) [11,12], collective modes

such as giant dipole resonances [13], and heavy-ion collisions [14,15]. Typically, experimental constraints are in the range $e_{\text{sym}}(n_{\text{sat}}) \approx 29$–$35$ MeV [9,16,17] at the nuclear saturation density, 0.16 fm$^{-3} \equiv n_{\text{sat}}^{\text{emp}}$ (for a review see, e.g., Ref. [14]). The determination of the symmetry energy is on the road-map for several future experiments conducted at rare-isotope beam facilities such as FRIB at MSU, SPIRAL2 at GANIL, and FAIR at GSI. While there are nuclear EOS models for a wide range of values for the symmetry energy and its density dependence [18,19], microscopic EOS calculations based on chiral nuclear interactions have improved theoretical constraints considerably over the last years (see, e.g., Refs. [3,20,21] for recent reviews).

An extraction of the nuclear symmetry energy from nuclear theory as well as experimental and astrophysical programs requires that the measured quantities in these different approaches, as well as their relations, are well defined. Different approximations for the symmetry energy are commonly used. It is, therefore, important to clarify whether the symmetry energy measured in laboratory experiments is the same quantity as that inferred from NS properties. For example, the energy per particle of nuclear matter at zero temperature is a function of the baryon density $n = n_n + n_p$ and isospin asymmetry $\delta = (n_n - n_p)/n$, where n_n (n_p) denotes the neutron (proton) number density. The isospin-asymmetry expansion from symmetric nuclear matter (SNM, $\delta = 0$) to pure neutron matter (PNM, $\delta = 1$) is often employed,

$$e(n, \delta) \approx e(n, \delta = 0) + \delta^2 e_{\text{sym},2}(n) + \delta^4 e_{\text{sym},4}(n) + O(\delta^6).$$

(1)

*somasundaram@ip2i.in2p3.fr
†cdrischler@berkeley.edu
‡itews@lanl.gov
§j.margueron@ip2i.in2p3.fr

Here $e_{\text{sym,2}}(n)$ and $e_{\text{sym,4}}(n)$ are the quadratic and quartic contributions to the symmetry energy, respectively. Given the expansion (1), the quadratic contribution to the symmetry energy is defined by the second derivative

$$e_{\text{sym,2}}(n) = \frac{1}{2} \frac{\partial^2 e(n,\delta)}{\partial \delta^2}\bigg|_{\delta=0}, \qquad (2)$$

similar to the empirical Bethe-Weizsäcker mass formula for finite nuclei. Hence, $e_{\text{sym,2}}(n)$ is often referred to as the *symmetry energy* and is used in nuclear experiments. In practice, however, the more commonly used definition of the symmetry energy is given by the difference between the energy per particle in PNM and SNM,

$$e_{\text{sym}}(n) = e_{\text{PNM}}(n) - e_{\text{SNM}}(n). \qquad (3)$$

While definition (3) requires the EOS only in the limits of PNM and SNM, Eq. (2) necessitates explicit calculations of isospin-asymmetric nuclear matter (ANM). Both $e_{\text{sym,2}}(n)$ and $e_{\text{sym}}(n)$ are equal if the isospin dependence of the energy per particle is *purely* quadratic, i.e., nonquadratic terms in the expansion (1) vanish. However, there is no *a priori* argument why this should be the case. In fact, nonquadratic terms have been found to be relevant for, e.g., accurate studies of nuclear matter in beta-equilibrium at supra-saturation density [22–25] and the crust-core transition density in NSs [24,26].

In this work, we confront the expansion (1) with the explicit ANM calculations based on chiral nucleon-nucleon (*NN*) and three-nucleon (*3N*) interactions reported in Ref. [27] and quantify the impact of nonquadratic contributions to the symmetry energy. We also investigate to which extent uncertainties in the microscopic approach affect the extraction of nonquadratic contributions to the symmetry energy. The paper is organized as follows: In Sec. II, we give an overview of previous studies of nonquadratic contributions to the symmetry energy. In Sec. III, we present our computational setup and, in Sec. III A, we compare it with other calculations. In Sec. III B, the derivation of the Landau effective mass from the single-particle energy is presented. General expressions for the energy expansion in terms of the isospin-asymmetry parameter δ are given in Sec. III C, in particular, for the total energy per particle as well as for the contributions of the potential-energy terms. We then discuss the EOS in the limits of PNM and SNM in Sec. IV, followed by the symmetry energy in Sec. V. In Sec. VI, we study the impact of the nonquadratic contributions to the symmetry energy in determinations of the core-crust transition in NSs. Finally, we conclude in Sec. VII. The Python codes used to perform the analysis and generate the figures in this paper are publicly available on GitHub [28] and briefly described in the Supplemental Material [29] associated with this publication.

II. PREVIOUS STUDIES OF NONQUADRATIC CONTRIBUTIONS

As stated above, there is no *a priori* reason for the isospin-asymmetry expansion to be purely quadratic. In general, even

the free Fermi gas (FFG) energy per particle, given by

$$e^{\text{FFG}}(n) = \frac{t_{\text{SNM}}^{\text{sat}}}{2}\left(\frac{n}{n_{\text{sat}}}\right)^{2/3}[(1+\delta)^{5/3} + (1-\delta)^{5/3}], \qquad (4)$$

with $t_{\text{SNM}}^{\text{sat}} = \frac{3}{5m_N}(\frac{3\pi^2}{2}n_{\text{sat}})^{2/3} \approx 22.1$ MeV, leads to non-quadratic contributions to the expansion (1). For example, the quartic term,

$$e_{\text{sym,4}}^{\text{FFG}}(n) \simeq 0.45 \text{ MeV} \times \left(\frac{n}{n_{\text{sat}}}\right)^{2/3}, \qquad (5)$$

represents a $\approx 3.5\%$ correction to the FFG symmetry energy at n_{sat}. Nuclear interactions also contribute to nonquadratic terms; for example, the phenomenological Skyrme interaction [30] gives the following quartic contribution to the symmetry energy:

$$e_{\text{sym,4}}^{\text{Skyrme}}(n) \simeq e_{\text{sym,4}}^{\text{FFG}}(n) + \frac{k_F^5}{972\pi^2}[3t_1(1+x_1) + t_2(1-x_2)], \qquad (6)$$

where k_F is the Fermi momentum. The Skyrme parameters (t_1, t_2) represent the correction to the bare nucleon mass generated by in-medium effects. Since the Skyrme in-medium mass is generally $\approx 30\%$–40% lower than the bare mass [30], these terms increase the $e_{\text{sym,4}}^{\text{FFG}}$ by $\approx 30\%$–40% to $\approx (0.7$–$0.8)$ MeV. In a recent work, Cai and Li [25] found $e_{\text{sym,4}}(n_{\text{sat}}) = (7.2 \pm 2.5)$ MeV, which indicates a rather significant difference between e_{sym} and $e_{\text{sym,2}}$. They employed an empirically constrained isospin-dependent single-nucleon momentum distribution and the EOS of PNM near the unitary limit. Subsequently, Bulgac *et al.* found that $e_{\text{sym,4}}(n = 0.1 \text{ fm}^{-3}) = 2.635$ MeV is necessary in order to reproduce properties of both finite nuclei and the PNM EOS, as calculated in Ref. [31]. In contrast, previous works, e.g., based on Brueckner-Hartree-Fock (BHF) approaches and hard-core interactions [32–35] obtained only small nonquadratic contributions to the symmetry energy.

In a recent study of nuclear matter in many-body perturbation theory (MBPT) with contributions from 1π-exchange, 2π-exchange, and three-body terms involving virtual $\Delta(1232)$ isobars, Kaiser [36] could not confirm such large values for $e_{\text{sym,4}}$. Instead, Kaiser found $e_{\text{sym,4}} \simeq 1.5$ MeV at n_{sat}, which is still about three times larger than the FFG contribution. Moreover, Kaiser found contributions to the energy per particle whose fourth derivative with respect to δ are singular at $\delta = 0$. This was further substantiated by analytic MBPT calculations based on an *S*-wave contact interaction, which gave rise to a singular term $\propto \delta^4 \log|\delta|$—a term that only contributes to the ANM EOS when $\delta \neq 0$ and $\delta \neq 1$, and which will be referred to as the leading-order logarithmic term in the following.

Subsequently, Wellenhofer *et al.* performed a more detailed analysis of such divergences by examining the δ dependence of the nuclear EOS as a function of density and temperature [37]. They found that the asymmetry expansion is hierarchically ordered, i.e., the lower-order coefficients are dominant at high temperature and low density, but the expansion diverges at $\delta = 0$ with alternating sign in the zero-temperature limit. Around saturation density, their results

TABLE I. Nonlocal N³LO NN and N²LO $3N$ interactions used in the MBPT calculations of Ref. [27]. The interactions are based on the N³LO NN potential EM 500 MeV [38] evolved to the SRG resolution scale λ. The low-energy couplings c_D and c_E were subsequently fit to the triton binding energy and the charge radius of ^{4}He in Ref. [39] for different combinations of λ and the $3N$ cutoff Λ_{3N}. The $3N$ two-pion exchange is governed by the πN low-energy couplings c_1, c_3, and c_4, which were taken from the NN potential, except for H7 which uses the values obtained from the NN partial-wave analysis (PWA) of Ref. [40]. Hamiltonian H6 has been excluded as discussed in Sec. IV B of Ref. [27].

Label	λ [fm^{-1}]	Λ_{3N} [fm^{-1}]	$3N$ $c_{1,3,4}$	c_D	c_E
H1	1.8	2.0	NN potential	$+1.264$	-0.120
H2	2.0	2.0	NN potential	$+1.271$	-0.131
H3	2.0	2.5	NN potential	-0.292	-0.592
H4	2.2	2.0	NN potential	$+1.214$	-0.137
H5	2.8	2.0	NN potential	$+1.278$	-0.078
H7	2.0	2.0	PWA [40]	-3.007	-0.686

indicate that the convergence of the series expansion is restored for $T \gtrsim 3$ MeV. Moreover, they have argued that the logarithmic term at leading order considerably improves the isospin-asymmetry expansion at zero temperature and suggested to include this term in future fits of the EOS.

While mathematically well-defined, it is not clear whether the aforementioned divergence of the series expansion in δ substantially impacts the practical usability of the expansion (1), because corrections remain small at nuclear densities. Our knowledge of the symmetry energy, and, more fundamentally, of the nuclear interaction itself, is limited by experimental precision and by the theoretical understanding of strongly interacting systems. As a consequence, while the series expansion in the isospin asymmetry can be determined with high accuracy when the nuclear interaction and the many-body treatment are fixed (with numerical limitations as discussed in Ref. [37]), current theoretical uncertainties reduce our ability to accurately determine high-order contributions in general. In this paper, we analyze the impact of these uncertainties on the determination of the symmetry energy.

III. NUCLEAR-MATTER EQUATION OF STATE

In this work, we use the explicit ANM calculations of Ref. [27] at zero temperature to study the importance of non-quadratic contributions to the symmetry energy. Specifically, we analyze their results obtained with the improved (angle averaging) approximation for normal ordering $3N$ forces and in a Hartree-Fock single-particle spectrum. The MBPT calculations in Ref. [27] are based on the set of six chiral NN and $3N$ interactions summarized in Table I. These interactions are also commonly used in nuclear-structure calculations [41–50]. They combine the N³LO NN potential EM 500 MeV [38] evolved to lower momentum scales λ using the similarity renormalization group (SRG) with bare N²LO $3N$ forces regularized by a nonlocal regulator with momentum cutoff Λ_{3N}. Hebeler et $al.$ then fit the two $3N$ low-energy
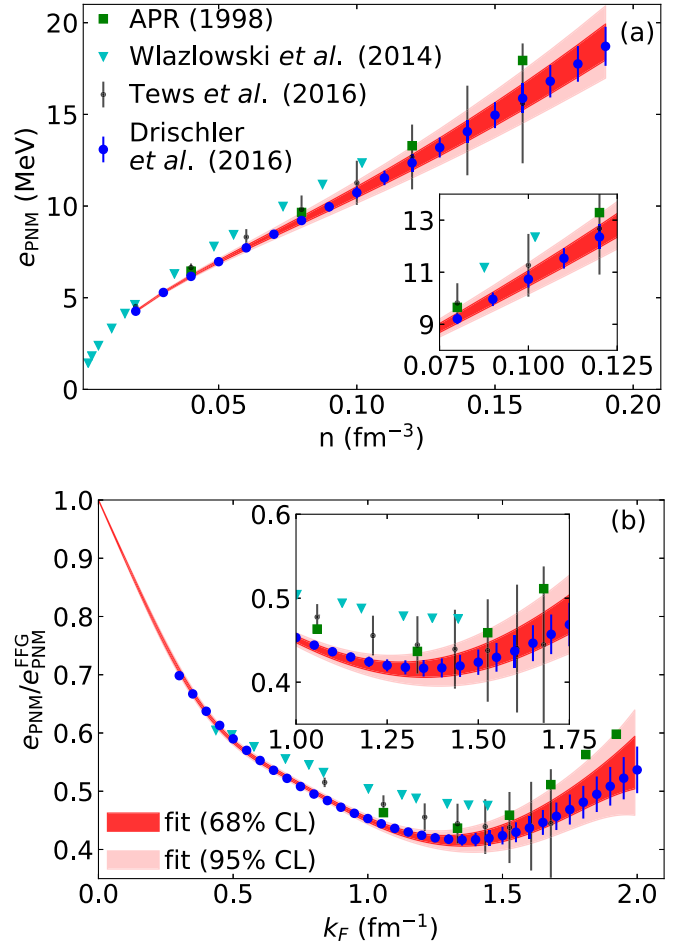

FIG. 1. Comparison of the MBPT predictions for the (a) energy per particle in PNM [27] (blue points) with the APR EOS [51] (green squares), QMC calculations Wlazlowski et $al.$ (2014) [31] (cyan triangles), and Tews et $al.$ (2016) [52] (black dots) using different chiral EFT Hamiltonians with NN and $3N$ forces. The latter points include simple estimates for the EFT truncation error of the chiral expansion. We also show our fit posterior at 68% (95%) confidence level as dark (light) red bands. (b) The same comparison but with a different scaling.

couplings c_D and c_E for the different combinations of λ and Λ_{3N} shown in Table I to the triton binding energy as well as the charge radius of ^{4}He [39]. Assuming N²LO $3N$ forces provide a sufficiently complete operator basis, and the long-range low-energy couplings c_1, c_3, and c_4 are SRG-invariant, this approach captures dominant contributions from induced three-body forces due to the SRG transformation. Note that the c_i appear both in the NN and $3N$ interactions at N²LO. As discussed in Ref. [27], the spread in the energy per particle obtained from these nuclear interactions can serve as a simple uncertainty estimate—though with limited statistical meaning.

A. Energy per particle

The energy per particle in PNM obtained in Ref. [27] is depicted in the upper panel of Fig. 1 by blue dots (the

lower panel represents the ratio of the energy per particle over the FFG energy). In this work, we perform least-squares fits of nonlinear functions to the MBPT data. Each fit parameter is guided by a (Bayesian) prior, which distinguishes our parametric fits[1] from a standard χ^2 minimization (see the Supplemental Material [29] for more details). The parametric fits result in the posterior distributions shown as dark (light) red bands corresponding to 68% (95%) confidence intervals in Fig. 1.

In Fig. 1, we also provide comparisons with the variational calculation of Ref. [51] (APR), Fock-space formulated quantum Monte Carlo (QMC) calculations of Ref. [31] (Wlazlowski *et al.* 2014), and continuum QMC calculations using auxiliary field diffusion Monte Carlo of Ref. [52] (Tews *et al.* 2016). These calculations were not only conducted using different many-body approaches, but also different nuclear interactions: the APR result uses the Argonne v_{18} (AV18) *NN* potential [54] and the Urbana IX (UIX) 3*N* force [55], Ref. [31] employs the nonlocal momentum-space chiral N^{3}LO *NN* interactions of Ref. [56] combined with N^{2}LO 3*N* forces as specified in Ref. [57], and Ref. [52] uses local coordinate-space chiral interactions constructed in Refs. [58–60]. The first two calculations do not provide theoretical uncertainties, while the latter estimates the standard EFT uncertainty [61]. Note that, in general, order-by-order calculations are required for estimating EFT truncation errors. Such calculations are not possible with the chiral Hamiltonians given in Table I.

When comparing the approaches using chiral EFT interactions, the QMC calculations of Ref. [52] agree with the MBPT approach employed in this work within uncertainties above $n \approx 0.08$ fm^{-3}, while QMC finds slightly higher energies at lower densities. In contrast, the QMC calculations of Ref. [31] find a higher PNM energy per particle at all densities, by about ≈ 1 MeV. We also compare the ratio $e_{\text{PNM}}/e_{\text{PNM}}^{\text{FFG}}$ as a function of neutron Fermi momentum k_{F} for the various calculations in the bottom panel of Fig. 1. In the figure, we can identify the density region where the ratio exhibits a plateau, indicating a similar scaling of e_{PNM} and e^{FFG} with k_{F}. For the MBPT calculation, we find the ratio at the plateau to be $\approx 0.42(1)$ in PNM at momenta $k_{\text{F}} \approx 1.3(2)$ fm^{-1}, which describes densities at $\approx n_{\text{sat}}/2$.

The comparison of the different results in Fig. 1 provides a qualitative illustration of the uncertainties originating from the nuclear interactions as well as from the different many-body approaches. While the MBPT results of Ref. [27] provide a simple uncertainty estimate, they do not quantify EFT truncation errors, which can be significant at $n \gtrsim n_0$. Future order-by-order calculations of ANM will enable statistically robust EFT uncertainty estimates using the Bayesian framework recently developed by the BUQEYE collaboration [62,63]. In the present analysis, however, such systematic ANM calculations are not available. Therefore, we follow the approach in Ref. [27] and consider the spread of the EOSs due to the Hamiltonians in Table I as an uncertainty estimate.

---

[1]These fits were performed using the LSQFIT Python package [53].

B. Landau mass contribution to the symmetry energy

Nontrivial contributions to the symmetry energy can arise due to the effective mass, see for instance Eq. (6). Therefore we characterize these effects here before commencing our analysis of the energy per particle. For this purpose we start with the single-particle energy $\epsilon_\tau(k)$ in a Hartree-Fock spectrum (as in Ref. [27]),

$$\epsilon_\tau(k, n, \delta) \approx \frac{k^2}{2m_\tau} + \Sigma^{(1)}(k, n, \delta). \qquad (7)$$

The first term in Eq. (7) is the single-particle kinetic energy, while the second term $\Sigma^{(1)}$ denotes the spin-isospin-averaged first-order self-energy. We refer the reader to, e.g., Refs. [27,64] for more details.

The momentum dependence of the nuclear interactions can be absorbed by modifying the nucleon mass, which gives rise to the so-called in-medium effective mass and the Landau mass. Specifically, Eq. (7) can be approximated as

$$\epsilon_\tau(k, n, \delta) \approx \frac{k^2}{2m_\tau^*(k, n, \delta)} + \Sigma^{(1)}(k = 0, n, \delta), \qquad (8)$$

where the in-medium effective mass is defined as [65]

$$\frac{m_\tau^*(k, n, \delta)}{m_\tau} = \frac{k}{m_\tau} \left(\frac{d\epsilon_\tau(k, n, \delta)}{dk} \right)^{-1}. \qquad (9)$$

Finally, the Landau mass is defined as the effective mass (9) evaluated at $k = k_{\text{F}}$.

Several comments regarding the features of the single-particle energies, the in-medium effective mass, and the Landau effective mass are given in Appendix A. Here, we focus on the description of the Landau mass as a function of the density n and asymmetry parameter δ. We consider the following functional form:

$$\left(\frac{m_\tau^*}{m}(n, \delta) \right)^{-1} = 1 + \left(\frac{\kappa_{\text{sat}}}{n_{\text{sat}}} + \tau_3 \delta \frac{\kappa_{\text{sym}}}{n_{\text{sat}}} \right) n$$
$$+ \left(\frac{\kappa_{\text{sat},2}}{n_{\text{sat}}^2} + \tau_3 \delta \frac{\kappa_{\text{sym},2}}{n_{\text{sat}}^2} \right) n^2, \qquad (10)$$

where $\tau_3 = 1 (-1)$ for neutrons (protons). Note that we have neglected terms of higher order in δ in Eq. (10). The parameters κ_{sat}, $\kappa_{\text{sat},2}$, κ_{sym}, and $\kappa_{\text{sym},2}$ are obtained from fitting the expression (10) (in SNM and PNM) to the results computed using Eq. (9). The details of our parametric fits is discussed in the Supplemental Material [29]. The relevant fit parameters, p_α, are

$$p_\alpha = \left\{ \kappa_{\text{sat}}/n_{\text{sat}}, \ \kappa_{\text{sat},2}/n_{\text{sat}}^2, \ \kappa_{\text{PNM}}/n_{\text{sat}}, \ \kappa_{\text{PNM},2}/n_{\text{sat}}^2 \right\}. \qquad (11)$$

These fit parameters are determined from the predicted Landau effective masses for each of the six Hamiltonians. The results of the fits for the inverse of the Landau mass are given in Table II, where we have considered both, a linear and a quadratic fit function. The prior distribution for each of the fit parameters is given by a normal distribution with mean 0 and standard deviation 100, providing an uninformative prior. The fits are compared with three Skyrme-type interactions: NRAPR [4], LNS5 [66], and SAMI [67] that satisfy the

TABLE II. Fit parameters of the inverse Landau mass considering linear and quadratic density expansions. The fits are compared with three Skyrme-type interactions: NRAPR [4], LNS5 [66], and SAMI [67].

	$\kappa_{\text{sat}}/n_{\text{sat}}$ [fm^3]	$\kappa_{\text{sat,2}}/n_{\text{sat}}^2$ [fm^6]	$\kappa_{\text{PNM}}/n_{\text{sat}}$ [fm^3]	$\kappa_{\text{PNM,2}}/n_{\text{sat}}^2$ [fm^6]
Linear	3.33(18)		0.89(19)	
Quadratic	6.25(35)	−16.9(16)	2.63(14)	−11.1(19)
NRAPR [4]	2.75		1.40	
LNS5 [66]	4.12		2.19	
SAMI [67]	3.03		2.87	

following conditions: $0.6 \leqslant m^*/m(\text{SNM}) \leqslant 0.7$, $\Delta m^*/m > 0$, and $40 \text{ MeV} < L_{\text{sym}} < 60 \text{ MeV}$.

In Fig. 2, we compare the posterior distribution functions for the Landau mass in SNM (top panel) and PNM (bottom panel), and the input data. The predictions from the six Hamiltonians are plotted as solid lines, and, at each density, we
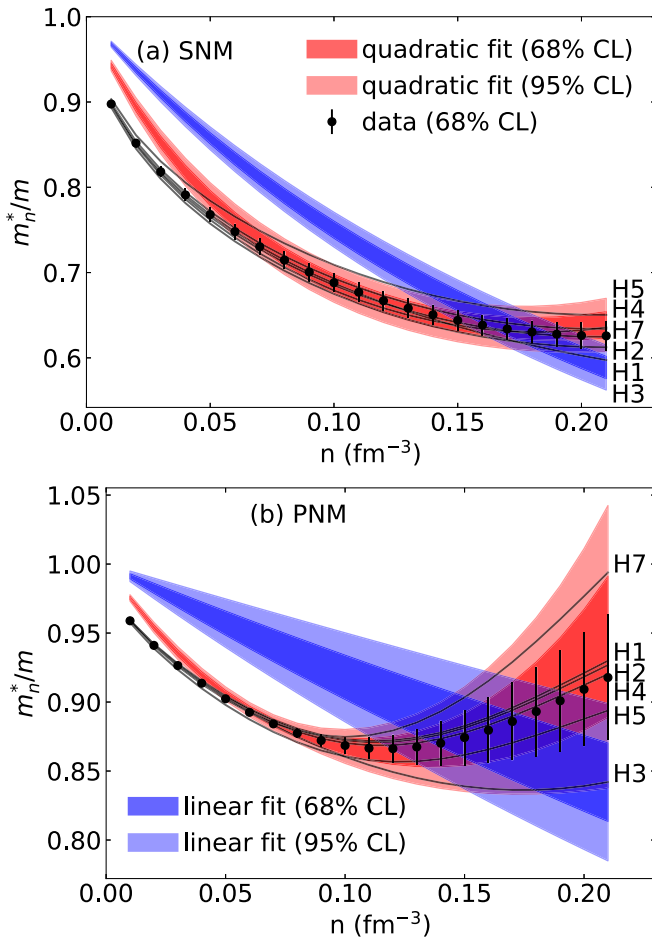

FIG. 2. Results of the Bayesian parametric fits of the Landau mass in (a) SNM and (b) PNM. The 68% (95%) confidence levels for the posterior distribution functions are shown as dark-shaded (light-shaded) bands. The black lines represent the individual Hamiltonians, and the black points show the average over the six Hamiltonians with ±1σ uncertainty bands.

calculate the centroid and 1σ interval given the six Hamiltonians (black points with error bars). The $\pm 1\sigma$ ($\pm 2\sigma$) contours of the posterior, corresponding to the 68% (95%) confidence region, are depicted in red (light red) for the quadratic fit and dark blue (light blue) for the linear fit. We fit the models to the data in the range $n = 0.15$–0.17 fm^{-3} for the linear fit (three data points) and from $n = 0.07$–0.20 fm^{-3} for the quadratic fit (14 data points). These values are chosen to allow for the ranges to be as large as possible while, at the same time, ensuring that the fits reproduce the data around saturation density. While the quadratic fit performs well even outside the fit interval, down to $n \approx 0.05$ fm^{-3} in SNM and PNM, the linear fit does not because of the strong curvature of the Landau mass. The differences between the linear and quadratic fits are further analyzed in Sec. V.

The fact that the Landau mass induces nontrivial contributions to the symmetry energy can be seen by explicitly including it in the effective kinetic energy

$$t^*(n, \delta) = \frac{t_{\text{SNM}}^{\text{sat}}}{2} \left(\frac{n}{n_{\text{sat}}} \right)^{2/3}$$
$$\times \left[\frac{m}{m_n^*(\delta)} (1 + \delta)^{5/3} + \frac{m}{m_p^*(\delta)} (1 - \delta)^{5/3} \right]. \quad (12)$$

We will now present our generalized framework to analyze the EOS, using the Landau mass appearing in Eq. (12), in the following subsection.

C. Energy expansion in the isospin asymmetry parameter δ

A general expression for the expansion (1) of energy observables in nuclear matter was suggested in Ref. [37], from which we consider all contributions up to δ^4, including the logarithmic term, and rewrite it as

$$y(n, \delta) \approx y_{\text{SNM}}(n) + y_{\text{sym,2}}(n)\delta^2 + y_{\text{sym,4}}(n)\delta^4$$
$$+ y_{\text{sym,log}}(n)\delta^4 \log |\delta|, \quad (13)$$

see Eq. (27) of Ref. [37] for more details. In the following, we treat this expression as a parametrization of the EOS's δ dependence, in which the coefficients are determined by parametric fits, rather than a formal expansion in δ. The term $y_{\text{sym,log,4}}\delta^4 \log |\delta|$ originates from the second-order contribution in the many-body expansion, as explained in Ref. [37].

The corresponding contribution to the symmetry energy y_{sym} is defined as

$$y_{\text{sym}}(n) = y_{\text{PNM}}(n) - y_{\text{SNM}}(n). \quad (14)$$

The nonquadratic contribution to the symmetry energy is defined as

$$y_{\text{sym,nq}}(n) = y_{\text{sym}}(n) - y_{\text{sym,2}}(n). \quad (15)$$

Note that, since the logarithmic term vanishes in SNM and PNM, it also does not contribute to the nonquadratic term (15).

The quantity y in Eq. (13) can be the energy per particle e, as originally suggested by Kaiser [36], or any other energy contribution. For instance, it can be the potential energy

$y = e^{\text{pot}}$ or the effective potential energy $y = e^{\text{pot}*}$ defined as

$$e^{\text{pot}}(n, \delta) = e(n, \delta) - t(n, \delta), \tag{16}$$

$$e^{\text{pot}*}(n, \delta) = e(n, \delta) - t^*(n, \delta), \tag{17}$$

where t and t^* are the kinetic and effective kinetic energy, see Eq. (12), respectively. In the following, we use these notations for analyzing the δ-dependence of the total, potential, and effective potential energies.

IV. META-MODEL FOR SYMMETRIC AND NEUTRON MATTER

To describe the MBPT data for the energy per particle in SNM and PNM, we use in this work a functional form described by a meta-model (MM) for nuclear matter similar to the one suggested in Ref. [17], but generalized to a potential energy with nonquadratic δ dependence. The MM is adjusted to MBPT data sampled on a given grid in the asymmetry parameter δ [27]. This is in contrast to Ref. [37], who used a finite-difference method [68] on an adjustable grid to determine all derivatives with respect to the δ of interest. The MM, instead, provides a flexible polynomial-type approach to nuclear matter, which allows us to accurately determine the higher-order coefficients in the δ expansion, even for the fixed grid considered here.

For SNM and PNM, the energy per particle in the MM reads

$$e_\alpha^{\text{MM}}(n) = t_\alpha^*(n) + e_\alpha^{\text{pot}*}(n), \tag{18}$$

where α stands for either SNM or PNM. The kinetic energy is determined by Eq. (12) with the Landau mass, see Sec. III B. The potential energies are expanded about n_{sat} in terms of the parameter

$$x \equiv \frac{n - n_{\text{sat}}}{3n_{\text{sat}}}$$

as follows:

$$e_{\text{SNM}}^{\text{pot}*}(n) = \sum_{j=0}^{N} \frac{1}{j!} v_{\text{SNM},j} x^j + v_{\text{SNM}}^{\text{low-n}} x^{N+1} e^{-b_{\text{sat}} \frac{n}{n_{\text{sat}}^{\text{emp}}}},$$

$$e_{\text{PNM}}^{\text{pot}*}(n) = \sum_{j=0}^{N} \frac{1}{j!} v_{\text{PNM},j} x^j + v_{\text{PNM}}^{\text{low-n}} x^{N+1} e^{-b_{\text{PNM}} \frac{n}{n_{\text{sat}}^{\text{emp}}}},$$

where the second term on the right-hand side is a low-density correction. This correction represents the low-density contribution of all higher-order terms neglected in the summation, and scales like x^{N+1} at leading order, where N is the upper limit of the power in the density expansion. In the original nucleonic MM of Ref. [17], the low-density EOS correction was simply parametrized by a fixed coefficient $b = b_{\text{sat}} = b_{\text{PNM}} \approx 6.93$. In the improved MM considered here, we introduce two parameters (b_{sat} and b_{PNM}) controlling the density dependence of the low-density corrections in PNM and SNM separately. It was suggested in Ref. [17] that using an expansion up to $N = 4$ allows for the reproduction of the pressure and sound speed of about 50 known energy density functionals (EDFs) up to about $4n_{\text{sat}}$. In principle, it is not necessary to consider

such a high N in the present analysis. The inclusion of high-order contributions, however, affects the determination of the low-order ones, as discussed in Ref. [69], even if the data do not constrain the high-order terms themselves.

Imposing that the energies per particle vanish at $n = 0$ fm^{-3}, we obtain the following relations:

$$e_\alpha^{\text{pot}*}(n) = \sum_{j=0}^{N} \frac{1}{j!} v_{\alpha,j} x^j u_{\alpha,j}(x), \tag{19}$$

where

$$u_{\alpha,j}(x) = 1 - (-3x)^{N+1-j} e^{-b_\alpha n/n_{\text{sat}}^{\text{emp}}}, \tag{20}$$

α indicates either SNM or PNM, and the corresponding b_{sat} or b_{PNM}.

In the MM, the coefficients $v_{\alpha,1}$ to $v_{\alpha,N}$ are related to the nuclear empirical parameters (NEPs), such as E_{sat}, K_{sat}, E_{sym}, L_{sym}, etc. These relations between the MM parameters and the NEPs are given in Appendix B for both SNM and PNM. Here we only note that these relations represent another difference to the original nucleonic MM of Ref. [17], where the isovector coefficients were determined assuming a quadratic isospin-asymmetry dependence of the symmetry energy. The isovector contribution of the present MM is built on the global symmetry energy (3), which allows for possible nonquadratic contributions to the symmetry energy. These contributions will be estimated from the difference between the global symmetry energy and its quadratic contribution, as detailed in Sec. V.

In our MM there are five NEP in SNM, including n_{sat}, and five additional NEP in PNM. Considering the two parameters controlling the low-density EOS, b_{sat} and b_{PNM}, there is a total of 12 parameters that need to be determined. Note that these parameters carry uncertainties that reflect the current lack of knowledge of the nuclear EOS. In our Bayesian fits, we use the priors for the NEP from the analysis presented in Refs. [17,70] and summarized in Table III. Here, we additionally vary the parameters b_{sat} and b_{PNM} to reproduce the low-density behavior of the energy per particle in SNM and PNM.

We show the fitted parameters in Table III. Note that both the posterior and prior of each parametric fit is a normal distribution with mean value and standard deviation (printed in parentheses). The posteriors we obtain for the NEPs may depend on the exact representation of the data points, i.e., if the data are equidistant in n or k_{F}. To gauge the sensitivity to this choice, we investigate the following three possible data representations. Figure 3 shows the results for these so-called scalings.

Since we require our fit to provide a representation of low-density nuclear matter (with a fair weight for the low-density points) in order to fix b_{sat} and b_{PNM}, we adopt for scaling 1 the representation of e/e^{FFG} as a function of the Fermi momentum k_{F}. Scaling 1 provides the best representation for analyzing the low-density properties of the energy per particle because an equidistant grid in k_{F} leads to a very dense data set at low densities. Note that, as mentioned in Sec. III, the original MBPT data [27] are provided on an equidistant grid in k_{F}. The scaling of the y axis normalizes the energies to

TABLE III. Priors and posteriors of the NEP from analyses of SNM and PNM. We report results for the different scalings described in the text. Values within parentheses represent the error bars at the $\pm 1\sigma$ level. NEPs for the following three Skyrme-type interactions are given: NRAPR [4], LNS5 [66], and SAMI [67].

Scaling	n_{sat} (fm^{-3})	E_{sat} (MeV)	K_{sat} (MeV)	Q_{sat} (MeV)	Z_{sat} (MeV)	b_{sat}
Prior	0.160(10)	−15.50(100)	230(20)	−300(400)	1300(500)	0(50)
1	0.166(8)	−15.48(58)	211(14)	−573(133)	1055(474)	17(5)
2	0.163(8)	−15.07(57)	227(18)	−172(243)	1287(499)	9(5)
3	0.163(8)	−15.07(57)	227(18)	−172(243)	1287(499)	9(5)
3*	0.161(7)	−15.17(57)	226(18)	−306(186)	1324(497)	17[a]
NRAPR [4]	0.161	−15.85	226	−363	1611	
LNS5 [66]	0.160	−15.57	240	−316	1255	
SAMI [67]	0.159	−15.93	245	−339	1330	

Scaling	n_{sat} (fm^{-3})	E_{PNM} (MeV)	L_{PNM} (MeV)	K_{PNM} (MeV)	Q_{PNM} (MeV)	Z_{PNM} (MeV)	b_{PNM}
Prior		16.00(300)	50(10)	100(100)	0(400)	−500(500)	0(50)
1	0.166(8)[b]	16.61(93)	48(5)	40(37)	−320(224)	−388(494)	42(4)
2	0.163(8)[b]	16.30(93)	47(5)	75(40)	34(285)	−504(497)	15(9)
3	0.163(8)[b]	16.30(93)	47(5)	75(40)	34(285)	−504(497)	15(9)
3*	0.161(7)[b]	16.16(89)	46(5)	57(34)	−110(206)	−450(492)	42[a]
NRAPR [4]	0.161	18.33	65	108	−52	−236	
LNS5 [66]	0.160	15.29	57	130	−34	−416	
SAMI [67]	0.159	13.32	47	127	35	−873	

[a]Fixed parameter.

[b]Quoted values are the n_{sat} priors considered in PNM and obtained from SNM posteriors.

the same order of magnitude at all k_F. For scaling 2, we choose the representation of e/e^{FFG} on an equidistant grid in density. We use cubic splines to interpolate the energies per particle from the original Fermi momentum grid to a equally spaced density grid. By switching from the equidistant grid in momentum to one in density, scaling 2 reduces the
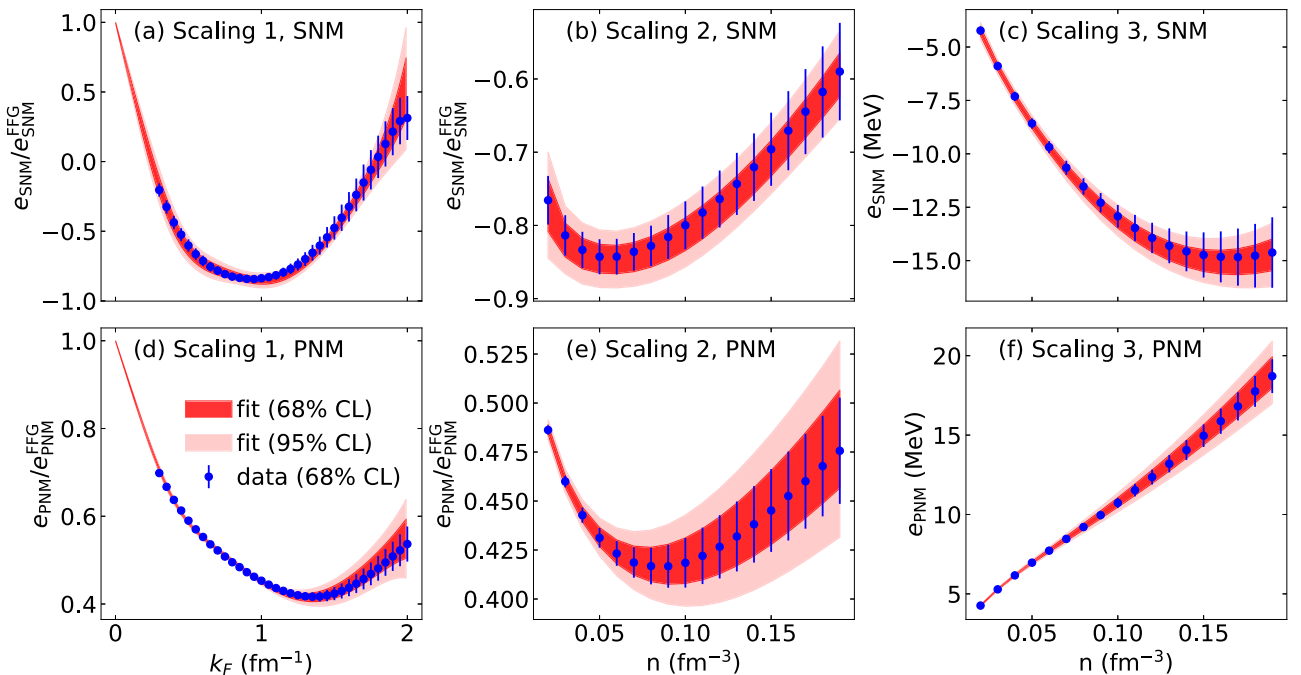

FIG. 3. Comparison of the Bayesian inference results for the MM of this work (red bands) with the MBPT data (blue points) for SNM [panels (a)–(c)] and PNM [panels (d)–(f)] and the three different scalings described in the main text. The bands are given at the 65% (dark-shaded) and 95% confidence level (light-shaded), whereas the data points are shown with the $\pm 1\sigma$ uncertainty estimate.

weight for the low-density data points and, therefore, is more appropriate to fit the NEPs, which are determined around saturation density. Finally, scaling 3 represents the energy per particle on an equidistant grid in density, as is more often presented in the literature. Hence, the only difference with scaling 2 is the normalization of the energy. The results for each of the three scalings are shown in Fig. 3 for SNM and PNM, while the posteriors for the NEPs are given in Table III. Note, that the NEP n_{sat} is only meaningful in SNM, while its uncertainty influences the determination of the NEPs in PNM. In our approach, we therefore vary n_{sat} in PNM within the posterior uncertainty obtained from the fit in SNM. In this way, the NEP in PNM naturally include the uncertainty in n_{sat}.

In the case of Scaling 1, when simultaneously varying the 12 MM parameters, we find $b_{SNM} = 17(5)$ and $b_{PNM} = 42(4)$ as well as the values for the 10 NEP given in Table III. The density dependence of the low-density correction is, thus, very different in SNM and PNM, in contrast with the original MM of Ref. [17]. We find some differences between the NEPs obtained from scaling 1 and scalings 2 and 3. These differences are usually small compared with the uncertainties, except for Q_{sat} in SNM, as well as Q_{PNM} in PNM. We note that the fits from scalings 2 and 3 are identical and, hence, the scaling of the energy with respect to e^{FFG} has a negligible effect.

Finally, we fix the values for b_{sat} and b_{PNM} from scaling 1, and refit all remaining NEP considering scaling 3. The results are referred to as scaling 3*. Fixing b_{SNM} and b_{PNM} has the largest impact on Q_{sat} and Q_{PNM}, as expected, but differences between scaling 3 and 3* are small compared with the overall uncertainties. Hence, we conclude that the parameters b_{SNM} and b_{PNM} do not have a significant impact on the determination of the NEPs and can be fixed from the fit to low-density matter (scaling 1). We stress that, for the higher-order NEPs Z_{sat} and Z_{PNM}, our analysis simply returns the prior, which implies that they are not constrained by our data. This is because the density range of the MBPT data is limited to densities $n \lesssim 0.21$ fm^{-3}. However, they contribute to the uncertainty of the other NEPs [69].

For the NEPs describing nuclear saturation we obtain from scaling 3 $n_{sat} = 0.161(7)$ fm^{-3}, $E_{sat} = -15.17(57)$ MeV, and $K_{sat} = 226(18)$ MeV. The results are consistent with the original analysis in Ref. [27], which obtained $n_{sat} = 0.143$–0.190 fm^{-3}, $E_{sat} = -(15.1$–$18.3)$ MeV, and $K_{sat} = 223$–254 MeV using a Hartree-Fock spectrum. However, our uncertainties are generally smaller because we explicitly guide the fits in Fig. 3 by empirical (or "expert") knowledge [17] through prior distributions of the fit parameters. In PNM, where empirical constraints are lacking, the fits are therefore closer to the MBPT data.

V. SYMMETRY ENERGY

Using the results obtained in Secs. III B and IV, we now determine the properties of the symmetry energy and the relative contributions of the quadratic and nonquadratic terms.

A. Global symmetry energy e_{sym}

The global symmetry energy e_{sym} is determined from our fits in PNM and SNM, see Eq. (3) and Sec. IV, and the contributions of the potential energies e_{sym}^{pot}, and e_{sym}^{pot*} are obtained from e_{sym} following:

$$e_{sym}^{pot}(n) = e_{sym}(n) - t_{PNM}(n) + t_{SNM}(n), \qquad (21)$$

$$e_{sym}^{pot*}(n) = e_{sym}(n) - t_{PNM}^*(n) + t_{SNM}^*(n). \qquad (22)$$

We use the fits of the Landau mass discussed in Sec. III B to determine t^*, including its uncertainties, as explained in the following.

We present these quantities in Fig. 4 as functions of the density n. For e_{sym}, the data points are obtained from the PNM and SNM data, and their uncertainties are defined by the arithmetic average of the PNM and SNM error bars. For the model, we employ the symmetry energy determined from the MM, which is defined as

$$e_{sym}^{MM}(n) = e_{PNM}^{MM}(n) - e_{SNM}^{MM}(n). \qquad (23)$$

The results shown in Fig. 4 are obtained from the best fits to SNM and PNM (scaling 3* in Table III), where the width of the bands is defined as the arithmetic average of the widths in SNM and PNM. The model results, therefore, depend on the choice of prior in SNM and PNM, in particular, on the prior knowledge of the saturation density and energy considered in SNM, see the discussion of Fig. 3. For this reason, the MM uncertainty for the symmetry energy is slightly smaller than the uncertainty of the data in Fig. 4. At nuclear saturation density, $n_{sat} = 0.161(7)$ fm^{-3}, the data suggest $e_{sym} = 30.70(140)$ MeV, while the MM leads to $e_{sym} = 31.33(106)$ MeV. Our values for the symmetry energy are in good agreement with the fiducial value of 31.6 ± 2.7 MeV in Ref. [71], with the recent Bayesian analysis in Refs. [62,63] that fully quantifies correlated EFT truncation errors with chiral NN and $3N$ interactions up to N^{3}LO, 30.9(11) MeV at the canonical saturation density, with the value of 30(3) MeV in Ref. [72] ($E\mathbb{1}$), and the range 29–35 MeV obtained in Ref. [73]. Similarly, we predict $L_{sym} = 46.2(49)$ MeV, while $L_{sym} = 58.9(160)$ MeV was found in Ref. [71], $L_{sym} = 58.4(48)$ MeV in Refs. [62,63] at the canonical saturation density, and the range $L_{sym} \in [43, 67]$ MeV in Ref. [73]. The determination of L_{sym}, however, is sensitive to the densities at which the value is extracted as well as to the interactions employed.

The data for e_{sym}^{pot} and e_{sym}^{pot*} are obtained from e_{sym} using Eqs. (21) and (22). In the case of e_{sym}^{pot*}, the effective mass is fixed to be the best fit using either the linear or the quadratic density expansion (depicted by dashed lines in the right panel), and the uncertainty of e_{sym}^{pot*} is defined as the arithmetic average of the uncertainties of e_{sym}, t_{PNM}^*, and t_{SNM}^*. Therefore, the uncertainty of e_{sym}^{pot*} also includes the uncertainties in the Landau mass parameters κ_{sat} and κ_{PNM}. We observe that there is a large impact of the Landau mass on e_{sym}^{pot*}, compared with e_{sym}^{pot} with the bare mass. At n_{sat}, we obtain $e_{sym}^{pot} = 18.1(7)$ MeV and $e_{sym}^{pot*} = 25.7(14)$ MeV. Hence, the Landau mass increases the potential part of the
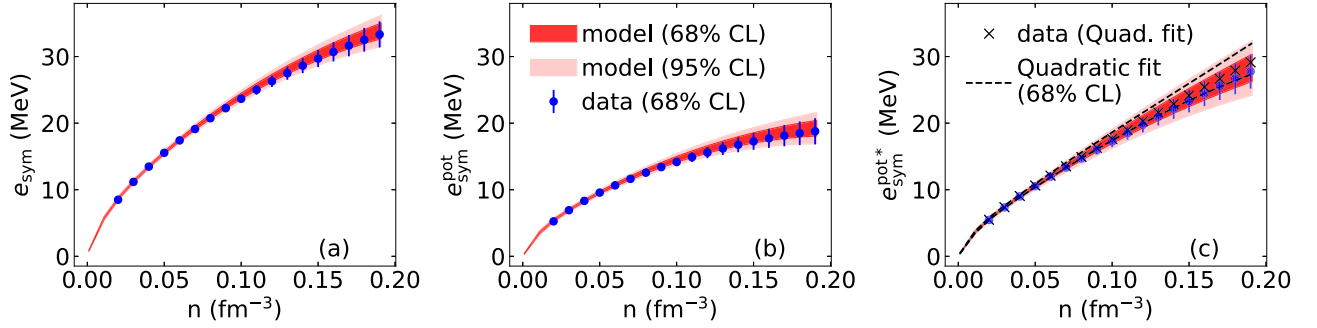
FIG. 4. Results for the (a) symmetry energy, $e_{\text{sym}}(n)$, (b) its potential contribution $e_{\text{sym}}^{\text{pot}}$, and (c) the effective potential $e_{\text{sym}}^{\text{pot*}}$ using (21) and (22). The meaning of the individual bands and points is the same as in Fig. 3. In the right panel, the light- and dark-shaded red bands and the data (blue points) correspond to calculations where the Landau mass is represented by a linear polynomial. The black squares (without error bars) and the black dashed lines (enclosing a band) represent calculations where the Landau mass is represented by a quadratic fit.

symmetry energy by about 30%–40% as discussed in the introduction. These numbers are compatible with the expectations for the complementary contribution from the kinetic energy. We find $t_{\text{PNM}}(n_{\text{sat}}^{\text{emp}}) - t_{\text{SNM}}(n_{\text{sat}}^{\text{emp}}) = 13.0$ MeV and $t_{\text{PNM}}^*(n_{\text{sat}}^{\text{emp}}) - t_{\text{SNM}}^*(n_{\text{sat}}^{\text{emp}}) = 5.4(13)$ MeV.

For $e_{\text{sym}}^{\text{pot*}}$, we expect a difference when using either a Landau mass that is linear or quadratic in density, see Fig. 2. In Fig. 4 we show two results for $e_{\text{sym}}^{\text{pot*}}$. The blue data points and the dark-shaded (light-shaded) red bands correspond to the results at 68% (95%) confidence level when using a Landau mass linear in density. The black squares and the black-dashed lines, encompassing the corresponding 68% confidence interval, represent calculations with a Landau mass quadratic in density. Interestingly, the values for $e_{\text{sym}}^{\text{pot*}}$ obtained from these two functions for the Landau mass differ only by about 1.8%, which is quite small. We, therefore, use only the linear fit for the Landau mass in the following.

B. Quadratic contribution to the symmetry energy

The quadratic contribution to the symmetry energy, $e_{\text{sym},2}$, is defined in Eq. (2) as the local curvature in the isospin-asymmetry parameter δ in SNM. In the following, we extract $e_{\text{sym},2}$ using this expansion around SNM but also suggest obtaining $e_{\text{sym},2}$ from an expansion around PNM. We demonstrate that both definitions provide comparable results.

1. Expansion around SNM

The quadratic contribution to the symmetry energy is defined by Eq. (2) relative to the SNM EOS. To determine this contribution directly from the MBPT data, we employ Eq. (1) up to the fourth order in δ, and fit the coefficients $e_{\text{sym},2}$ and $e_{\text{sym},4}$ using a standard least-squares minimization. The fits are performed in the range, $\delta = 0.0$–0.5. We have checked that the results are insensitive (within variations of about 0.1 MeV) to the upper limit of this range—as long as it is chosen to be $\delta \geqslant 0.5$.

For the model, we express $e_{\text{sym},2}(n)$ as a function of the density using the MM contribution to the quadratic symmetry energy,

$$e_{\text{sym},2}^{\text{MM}}(x) = \frac{5}{9}t_{\text{SNM}}(x) + \sum_{j=0}^{N} \frac{x^j}{j!}[v_{\text{sym2},j}u_j(x, \delta = 0)$$
$$- v_{\text{SNM,j}}[u_j(x, \delta = 0) - 1](1 + 3x)b_{\text{sym}}], \quad (24)$$

where the parameters $v_{\text{sym2},i}$ are determined using a Bayesian parametric fit (that was introduced in Sec. III A), as before for other quantities. Their relation to the quadratic symmetry energy NEPs are given in Appendix B. The parameter $b_{\text{sym}} \equiv b_{\text{PNM}} - b_{\text{SNM}}$ is fixed by the 3* fit.

The contributions to the symmetry energy due to the potential energy are determined from the following expressions:

$$e_{\text{sym},2}^{\text{pot}}(n) = e_{\text{sym},2}(n) - \frac{5}{9}t_{\text{SNM}}(n), \quad (25)$$

$$e_{\text{sym},2}^{\text{pot*}}(n) = e_{\text{sym},2}(n) - \frac{5}{9}t_{\text{SNM}}(n)\left[1 + (\kappa_{\text{sat}} + 3\kappa_{\text{sym}})\right.$$
$$\left. \times \left(\frac{n}{n_{\text{sat}}}\right) + (\kappa_{\text{sat},2} + 3\kappa_{\text{sym2}})\left(\frac{n}{n_{\text{sat}}}\right)^2\right]. \quad (26)$$

Our results for $e_{\text{sym},2}$, $e_{\text{sym},2}^{\text{pot}}$, and $e_{\text{sym},2}^{\text{pot*}}$ are shown in the first row of Fig. 5. At $n_{\text{sat}}^{\text{emp}}$, we find $e_{\text{sym},2}(n_{\text{sat}}^{\text{emp}}) = 30.0(4)$ MeV, $e_{\text{sym},2}^{\text{pot}}(n_{\text{sat}}^{\text{emp}}) = 17.7(4)$ MeV and $e_{\text{sym},2}^{\text{pot*}}(n_{\text{sat}}^{\text{emp}}) = 26.4(1.7)$ MeV (with the linear density-dependent model for the Landau mass). The large value of $e_{\text{sym},2}^{\text{pot*}}(n_{\text{sat}}^{\text{emp}})$, almost 90% of $e_{\text{sym},2}(n_{\text{sat}}^{\text{emp}})$, originates from the isospin dependence of the Landau mass, encoded by κ_{sym}.

From the fit model (24), we obtain an estimate for the NEPs that govern the quadratic contribution to the symmetry energy at the inferred value of n_{sat}. The values are given in the first row of Table IV. Our result for $E_{\text{sym},2}$ is about 1 MeV below the total symmetry energy, E_{sym}—the difference is due to nonquadratic contributions.

2. Expansion around PNM

An alternative approach is to determine the contribution $e_{\text{sym},2}$ from an expansion around PNM. Since the MBPT approach used here is able to explore asymmetric matter with
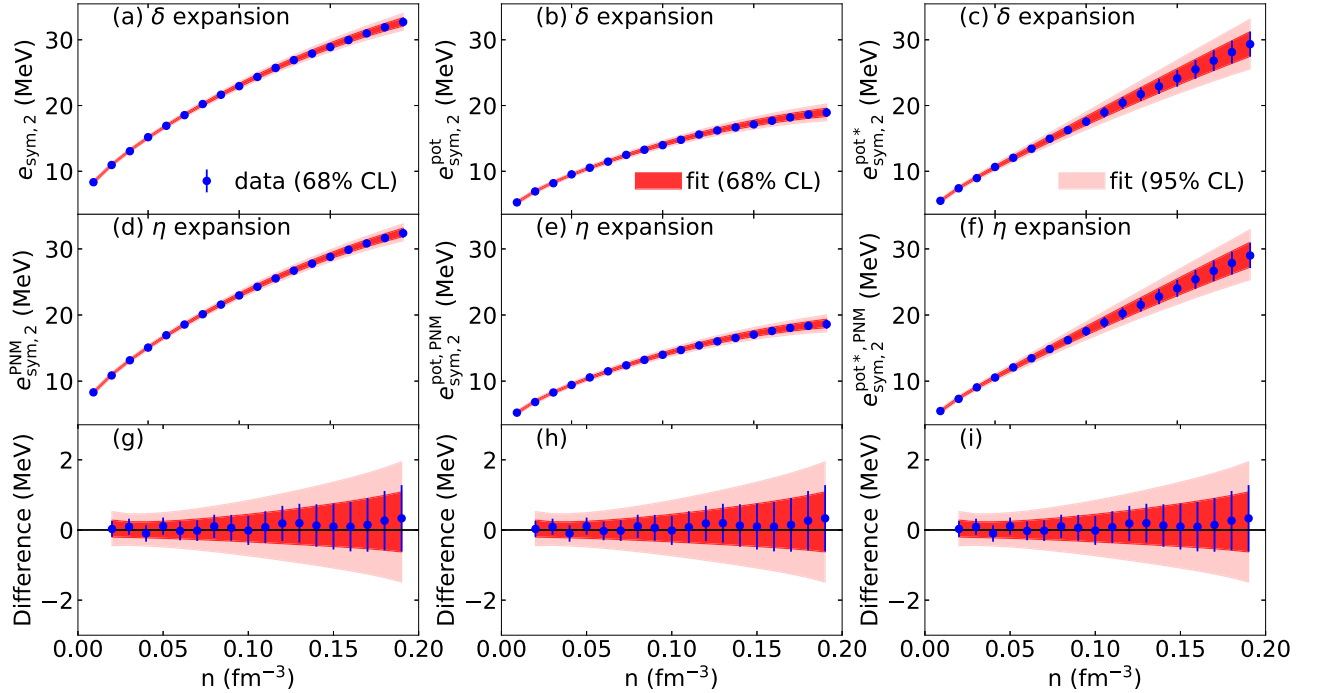
FIG. 5. Comparison of the extracted $e_{\mathrm{sym},2}$, $e_{\mathrm{sym},2}^{\mathrm{pot}}$, and $e_{\mathrm{sym},2}^{\mathrm{pot*}}$ using Eqs. (24)–(26) [panels (a)–(c)] and via an expansion around PNM, i.e., using Eq. (31) [panels (d)–(f)]. Panels (g)–(i) show the difference between the δ and η expansions.

arbitrary δ, we can test the accuracy of this alternative expansion.

To this end, we introduce the parameter

$$\eta = 1 - \delta = 2n_p/n, \qquad (27)$$

which is twice the proton fraction. Equation (1) can now be reexpressed in terms of the this parameter,

$$e(\eta) = e_{\mathrm{PNM}} - 2(e_{\mathrm{sym},2} + 2e_{\mathrm{sym},4})\eta + (e_{\mathrm{sym},2} + 6e_{\mathrm{sym},4})\eta^2$$
$$- 4e_{\mathrm{sym},4}\eta^3 + e_{\mathrm{sym},4}\eta^4 + O(\eta^5). \qquad (28)$$

From Eq. (28), it follows then

$$e_{\mathrm{sym},2}^{\mathrm{PNM}}(n) = -\frac{3}{4}\frac{\partial e}{\partial \eta}\bigg|_{\eta=0} - \frac{1}{4}\frac{\partial^2 e}{\partial \eta^2}\bigg|_{\eta=0}. \qquad (29)$$

We determine $e_{\mathrm{sym},2}^{\mathrm{PNM}}$ and $e_{\mathrm{sym},4}^{\mathrm{PNM}}$ from fitting the function

$$e(n, \eta) = e_{\mathrm{PNM}}(n) + a_1(n)\eta + a_2(n)\eta^2 + O(\eta^3), \qquad (30)$$

with

$$e_{\mathrm{sym},2}^{\mathrm{PNM}}(n) = -\frac{1}{4}[3a_1(n) + 2a_2(n)], \qquad (31)$$

$$e_{\mathrm{sym},4}^{\mathrm{PNM}}(n) = +\frac{1}{8}[a_1(n) + 2a_2(n)] \qquad (32)$$

at each density to the computed energies per particle at $\eta = 0.0, 0.1, 0.2$, and 0.3. Again, we also perform a Bayesian fit using Eq. (24). The two quantities are shown in the second row of Fig. 5, together with the potential terms $e_{\mathrm{sym},2}^{\mathrm{pot,PNM}}$ and $e_{\mathrm{sym},2}^{\mathrm{pot*,PNM}}$. The NEPs obtained from Eq. (24) are given in the second row of Table IV. Note that the differences between the NEPs extracted around SNM [using Eq. (2)] and around PNM

TABLE IV. Posteriors of empirical parameters obtained from the analysis of the δ and η expansions for $e_{\mathrm{sym},2}$. Values inside parentheses represent error bars at the $\pm 1\sigma$ level. Results for the following three Skyrme-type interactions are given: NRAPR [4], LNS5 [66], and SAMI [67].

Expansion	n_{sat} (fm^{-3})	$E_{\mathrm{sym},2}$ (MeV)	$L_{\mathrm{sym},2}$ (MeV)	$K_{\mathrm{sym},2}$ (MeV)	$Q_{\mathrm{sym},2}$ (MeV)	$Z_{\mathrm{sym},2}$ (MeV)	b_{sym}
Prior		31.50(350)	50(10)	−130(110)	−300(600)	−1800(800)	
δ (SNM)	0.161(7)[a]	30.16(83)	47(3)	−146(43)	90(334)	−1865(793)	25[b]
η (PNM)	0.161(7)[a]	30.02(82)	46(3)	−149(46)	93(352)	−1875(793)	25[b]
NRAPR [4]	0.161	32.78	60	−123	312	−1836	
LNS5 [66]	0.160	29.15	51	−119	286	−1672	
SAMI [67]	0.159	28.16	44	−120	372	−2180	

[a]Priors taken from the SNM posteriors in Table III.
[b]Fixed value.
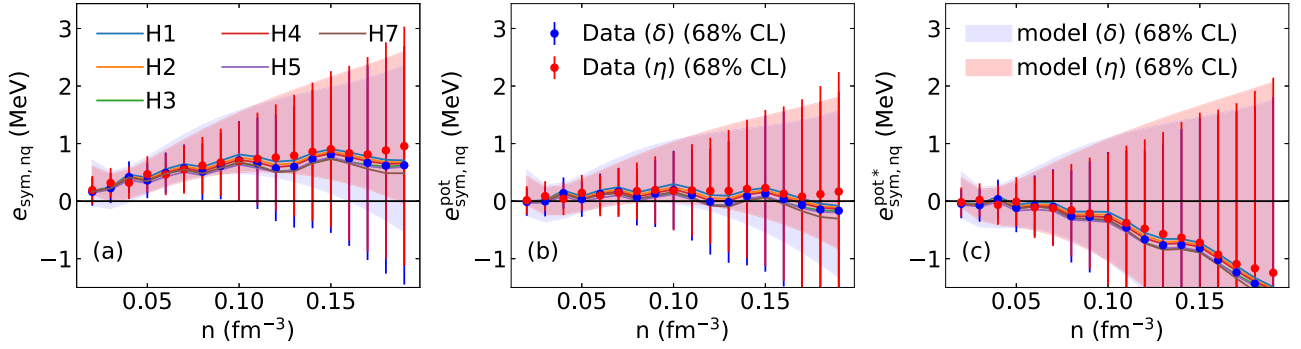
FIG. 6. Nonquadratic terms (a) $e_{\mathrm{sym,nq}}$, (b) $e_{\mathrm{sym,nq}}^{\mathrm{pot}}$, and (c) $e_{\mathrm{sym,nq}}^{\mathrm{pot*}}$ calculated via an expansion around SNM (blue) and PNM (red). For panel (c), the Landau mass is described by a linear fit. The colored lines depict results for the six individual Hamiltonians.

[using Eq. (29)] are much smaller than the uncertainties of these NEPs, which demonstrates that the two approaches are consistent with one another. This is further illustrated in the third row of Fig. 5, where the difference between $e_{\mathrm{sym,2}}^{\mathrm{SNM}}$ and $e_{\mathrm{sym,2}}^{\mathrm{PNM}}$ is shown to be consistent with zero and a small width of about 1.5 MeV at n_{sat}. Note that the width here is calculated as the arithmetic average of the widths of $e_{\mathrm{sym,2}}^{\mathrm{SNM}}$ and $e_{\mathrm{sym,2}}^{\mathrm{PNM}}$.

Determining the quadratic contribution to the symmetry energy from an expansion around PNM might be beneficial because PNM can usually be computed with much higher accuracy since the uncertainties in the $3N$ interactions are reduced. Furthermore, such an extraction is useful for microscopic approaches in which a small proton impurity can be treated more easily than SNM, e.g., the auxiliary-field diffusion Monte Carlo approach [72].

C. Nonquadratic contribution to the symmetry energy $e_{\mathrm{sym,nq}}$ and $e_{\mathrm{sym,4}}$

We now evaluate the contribution of the nonquadratic terms, defined by Eq. (15), using the expansions around SNM and PNM, respectively. For the global symmetry energy, we use our model (23), while for describing the quadratic contribution we use the fit (24). Figure 6 shows our results for the expansion around SNM (blue) and the expansion around PNM (red). Both expansions agree, and the differences are smaller than the uncertainties by a factor of two to three. We also show results for the six Hamiltonians. Their spread is much smaller than the uncertainties of the data or the model. This is because the latter are computed as arithmetic averages of the error bars of the global symmetry energy and the quadratic contribution. Such an average neglects the correlations between the two, leading to an overestimation of the error bars. At $n_{\mathrm{sat}}^{\mathrm{emp}}$, we obtain from our model $e_{\mathrm{sym,nq}} = 1.3(10)$ MeV, $e_{\mathrm{sym,nq}}^{\mathrm{pot}} = 0.6(10)$ MeV, $e_{\mathrm{sym,nq}}^{\mathrm{pot*}} = -0.5(22)$ MeV. For the individual Hamiltonians, we obtain $e_{\mathrm{sym,nq}} = 0.74_{-0.08}^{+0.11}$ MeV, $e_{\mathrm{sym,nq}}^{\mathrm{pot}} = 0.04_{-0.08}^{+0.11}$ MeV, $e_{\mathrm{sym,nq}}^{\mathrm{pot*}} = -1.02_{-0.08}^{+0.11}$ MeV, where the error bars are due to the different Hamiltonians.

We find that these nonquadratic contributions represent a correction of about 3%–5% to the symmetry energy. They originate mainly from the kinetic energy, since $e_{\mathrm{sym,nq}}^{\mathrm{pot}}$ remains close to zero across all densities. Our model estimates for the nonquadratic contributions to the symmetry energy and

the NEPs are summarized in Table V. We also compare the present NEPs to the three selected Skyrme interactions, showing a good agreement between the microscopic results and the EDF approaches.

We calculate the quartic contribution to the symmetry energy $e_{\mathrm{sym,4}}$ using Eq. (32), and show the resulting NEPs in Table V. We find that the quartic term to the symmetry energy accounts for about 60%–70% of the total nonquadratic contribution, while the remaining 30%–40% originate from higher-order contributions. The convergence of these additional contributions is discussed in Ref. [37]. We stress that this does not include any logarithmic contribution because such a contribution would vanish in PNM.

A recent analysis based on a general EDF approach—which was optimized to the properties of finite nuclei—concluded that quartic terms $\propto \delta^4$ have little impact on nuclei [74]. The result was interpreted as a consequence of the fact that the asymmetry δ in finite nuclei is small: for $Z > 8$ it varies between -0.33 and $+0.38$ in the latest Atomic Mass Data Center mass table AME2016 [75]. A quartic term was, however, found to be important to correctly reproduce the PNM energy per particle. To reproduce the PNM energy per particle predicted in Ref. [31], Ref. [74] found a quartic term of $e_{\mathrm{sym,4}} = 2.635$ MeV at $n = 0.1$ fm^{-3}. This term was the only nonquadratic contribution considered in Ref. [74] and is consistent within our upper 68% confidence interval for the nonquadratic contribution to the symmetry energy. The higher value for $e_{\mathrm{sym,4}}$ obtained in Ref. [74] might be related to the larger value in the PNM energy per particle obtained in Ref. [31], as shown in Fig. 1. This affects the symmetry energy because the contribution $e_{\mathrm{sym,4}}$ is needed to correctly reproduce the PNM EOS. Both the PNM energy per particle in Ref. [31] and $e_{\mathrm{sym,4}}$ obtained in Ref. [74] are ≈ 1 MeV higher than the values we obtain in the this work.

D. Logarithmic contribution to the symmetry energy $e_{\mathrm{sym,log}}$

The leading-order logarithmic contribution to the symmetry energy, see Eq. (13), was suggested to be of the form $\delta^4 \log|\delta|$ [36,37]. It therefore vanishes in both SNM and PNM, and data at finite isospin asymmetry are required to determine its magnitude. Such a logarithmic term would appear by a characteristic arch-like structure in the δ-dependent

TABLE V. Posteriors of nonquadratic and quartic NEPs obtained from the analysis of $e_{\text{sym,nq}}$ using the δ and η expansions, and $e_{\text{sym,4}}$ obtained from the η expansion only. For the extraction of $e_{\text{sym,nq}}$ via the η expansion, the values inside the square brackets are obtained from a fit to the data in order to provide a direct comparison to the corresponding analysis of $e_{\text{sym,4}}$. Values in parentheses represent the $\pm 1\sigma$ uncertainties. The NEPs for the following three Skyrme-type interactions are given: NRAPR [4], LNS5 [66], and SAMI [67].

Nonquadratic contribution	$E_{\text{sym,nq}}$ (MeV)	$L_{\text{sym,nq}}$ (MeV)	$K_{\text{sym,nq}}$ (MeV)	$Q_{\text{sym,nq}}$ (MeV)	$Z_{\text{sym,nq}}$ (MeV)
SNM	1.2(15)	0(6)	−24(58)	106(426)	91(1057)
PNM	1.3(15)	1(6)	−20(60)	103(441)	101(1058)
	[0.84(7)]	[0.7(8)]	[−9(13)]	[32(151)]	[167(958)]
NRAPR [4]	1.40	5	6	−1	−12
LNS5 [66]	1.70	6	9	−4	1
SAMI [67]	1.08	3	2	2	−24
Quartic contribution	$E_{\text{sym,4}}$ (MeV)	$L_{\text{sym,4}}$ (MeV)	$K_{\text{sym,4}}$ (MeV)	$Q_{\text{sym,4}}$ (MeV)	$Z_{\text{sym,4}}$ (MeV)
PNM	1.00(8)	0.6(6)	−7(12)	69(145)	33(956)
NRAPR [4]	0.95	3	4	−1	−6
LNS5 [66]	1.17	5	6	−4	3
SAMI [67]	0.70	2	2	1	−15

residuals between the data and a model without the logarithmic term. Figure 7 shows these residuals as a function of δ at three different densities. For asymmetric matter, we use

$$y^{\text{model}}(n, \delta) = y_{\text{SNM}}(n) + y_{\text{sym,2}}(n)\delta^2 + y_{\text{sym,nq}}(n)\delta^4, \quad (33)$$

where e_{SNM}, $e_{\text{sym,2}}$, and $e_{\text{sym,nq}}$ are given by Eqs. (18), (24), and (15). Note that, in the model (33), the fourth-order δ term

also includes possible higher-order contributions (like, for instance, a δ^6 term) contained in the term $y_{\text{sym,nq}}$. The different panels in Fig. 7 show the residuals at three densities, $n = 0.06$, 0.12, and 0.16 fm^{-3} (from the top to the bottom panel), and for the three choices for the variable y: e, e^{pot}, and $e^{\text{pot*}}$ (from left to right) as a function of the isospin asymmetry δ. The squares (shaded bands) represent the mean (68% confidence level) of
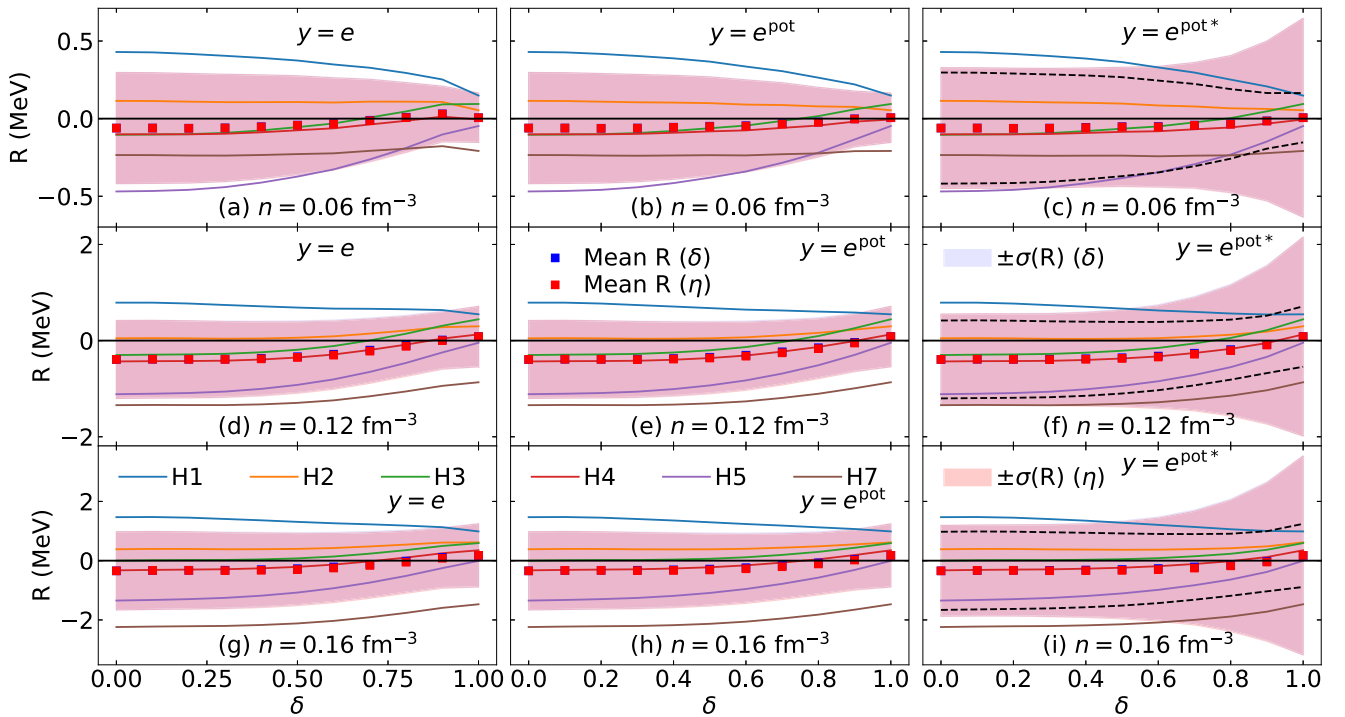

FIG. 7. Residuals R of the model, see Eq. (33), with respect to the data as a function of the asymmetry parameter δ for different values of the density: $n = 0.06$ fm^{-3} [panels (a)–(c)], $n = 0.12$ fm^{-3} [panels (d)–(f)], and $n = 0.16$ fm^{-3} [panels (g)–(i)]. The results are shown for the two different calculations of $y_{\text{sym,2}}$ and $y_{\text{sym,nq}}$—the expansions around PNM (red) and SNM (blue). The different columns correspond to e, e^{pot}, and $e^{\text{pot,*}}$. The colored lines depict the residuals of the fit for each Hamiltonian. In the last column, the black-dashed lines represent the upper and lower limits of the uncertainty in the residuals, respectively, by disregarding the uncertainties in the effective masses.
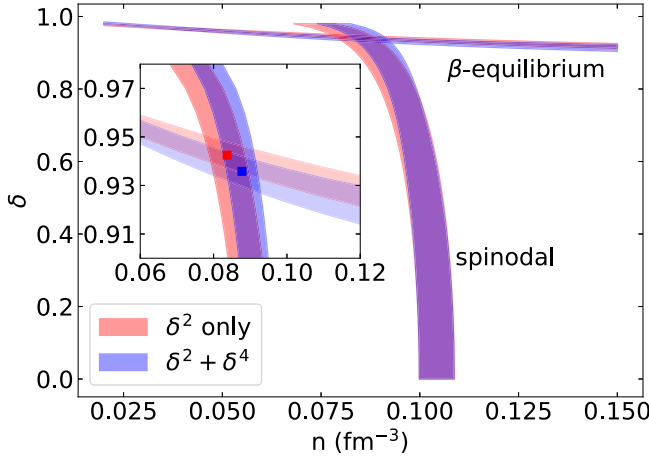
FIG. 8. Predictions for the spinodal density obtained by solving Eq. (34), and for beta equilibrium in low-density uniform matter by solving Eq. (35). The intersection denotes the crust-core transition, as indicated by a dot in the inset. The quadratic approximation (red band) is compared with the case where quartic contributions are included (blue band).

the residuals. The presence of logarithmic terms would appear as a systematic deviation of the these residuals from zero in asymmetric matter. However, this is not what we observe at the three considered densities and for all energy observables. Instead, we find the residuals to be compatible with zero and almost flat as a function of the isospin asymmetry. This is also the case for the results for each Hamiltonian, which we show as colored lines. The results for the individual Hamiltonians vanish on average, but the uncertainty bands remain quite sizable, about ±1–2 MeV around saturation density. Therefore, our findings suggest that there is no statistically significant indication for a net logarithmic contribution to the symmetry energy for the chiral *NN* and *3N* Hamiltonians used in this work.

Our conclusion about the strength of the logarithmic term is not in contradiction with the findings presented in

Refs. [36,37]. The logarithmic term in Ref. [37] was found to improve the description of the isospin dependence of the energy per particle by at most ≈0.1 MeV, shown for one Hamiltonian[2] in Fig. 9 of Ref. [37]. Such contributions of the order of ≈0.1 MeV are small compared with the overall theoretical uncertainties in this work, which we estimate by analyzing the six Hamiltonians in Table I.

VI. IMPACT ON THE NEUTRON-STAR CRUST-CORE TRANSITION

In this section, we study the impact of the nonquadratic contribution to the symmetry energy on the crust-core transition in neutron stars, for which the symmetry energy plays an important role [77–79]. This transition occurs at the core-crust transition density n_{cc} with an isospin asymmetry δ_{cc} that is determined by the beta-equilibrium. The parameters n_{cc} and δ_{cc} can be obtained from uniform matter by determining the density at which matter becomes unstable with respect to density fluctuations (spinodal instability) [77].

In multicomponent matter, e.g., matter that consists of neutrons and protons, this spinodal density is determined from the curvature (Hessian) matrix $\mathcal{C}$, defined as the second derivative of the energy density with respect to the component densities [77]. From the eigenvalues of $\mathcal{C}$, one can determine the stability of matter: if all eigenvalues are positive, i.e., if $\mathcal{C}$ is positive semidefinite, the matter exhibits a local stability against density fluctuations of all components in any combination, while a change of sign for any eigenvalue triggers an instability with respect to density fluctuations indicated by its associated eigenvector. The change of sign of the eigenvalues can be extracted from the determinant of $\mathcal{C}$, which reads in nuclear matter,

$$\det \mathcal{C}(n, \delta) = \frac{\partial \mu_n}{\partial n_n} \frac{\partial \mu_p}{\partial n_p} - \frac{\partial \mu_n}{\partial n_p} \frac{\partial \mu_p}{\partial n_n}, \qquad (34)$$

---

[2]This is the n3lo450 interaction constructed in Refs. [38,57,76], which is not considered in this work.

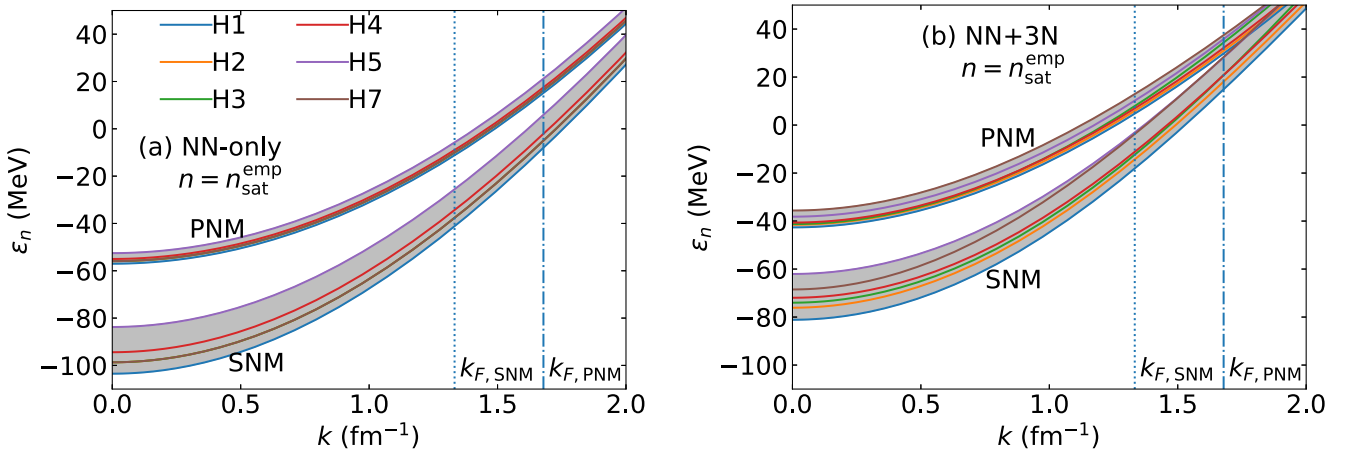

FIG. 9. The neutron single-particle energies $\epsilon_n(k)$ as a function of the momentum k calculated at $n_{\text{sat}}^{\text{emp}}$, and extracted from the MBPT calculations of Ref. [27]. The different colors correspond to the six Hamiltonians as labeled in the legend. We show the single-particle energies obtained from (a) only *NN* forces and (b) when including *3N* contributions. In each panel, we present results for both SNM and PNM.

TABLE VI. Crust-core transition density and isospin asymmetry, n_{cc} and δ_{cc}, respectively, for the purely quadratic case (δ^2 only) and for the case including the quartic contribution ($\delta^2 + \delta^4$), see Eq. (33).

Model	n_{cc} (fm^{-3})	δ_{cc}
δ^2 only	0.083(5)	0.944(5)
$\delta^2 + \delta^4$	0.087(4)	0.935(6)

where μ_n and μ_p are the neutron and proton chemical potentials. For simplicity, we have neglected the finite-size contribution from the Coulomb interaction as well as the gradient density terms induced by the finite range of nuclear interactions. It is expected that these terms reduce the spinodal density by only $\approx$0.01 fm^{-3} [77,79].

In subsaturation asymmetric matter, the equilibrium state is the state that satisfies the chemical-potential equilibrium $\mu_n = \mu_p + \mu_e$, at fixed baryon number $n = n_n + n_p$ and charge neutrality $n_e = n_p$. At zero temperature, and considering relativistic electrons, this system of equations reduces to a single nonlinear equation,

$$\sqrt{m_e^2 + \left(\frac{3\pi^2}{2}(1 - \delta_\beta)n\right)^{2/3}} = 2\frac{\partial e(n, \delta_\beta)}{\partial \delta}, \qquad (35)$$

whose solution, $\delta_\beta(n)$, is obtained by using a combination of the bisection and the secant methods implemented in the Python package of Ref. [80]. Then, we define the crust-core transition as the solution (n_{cc}, δ_{cc}) to both, the instability onset criterion, det $\mathcal{C} = 0$, and the beta equilibrium condition, e.g., Eq. (35). Equivalently, n_{cc} is defined as the spinodal density in beta equilibrium, where $\delta_{cc} = \delta_\beta(n_{cc})$. Figure 8 shows the intersection between these two determinations. We investigate the purely quadratic approximation for the symmetry energy, with the NEPs given in Table IV, and with the quartic terms from Table V included. For all cases, the reference MM in SNM is determined by the best fit given in Table III for the scaling 3*.

When we include quartic contributions, the spinodal density in neutron-rich matter is increased compared with the case where only the quadratic term is considered. This is because the quartic term increases the symmetry energy. For the same reason, the isospin asymmetry is decreased when nonquadraticities are included. Our results are summarized in Table VI and depicted in Fig. 8 by the blue and red points. They are in agreement with the predictions of, e.g., Refs. [78,79] with $L_{\text{sym},2} \approx 45$ MeV. From the comparison of our results with and without the quartic term, we find that the transition density changes by $\approx$5% while δ_{cc} changes by only $\approx$1%.

VII. SUMMARY AND CONCLUSIONS

We have analyzed the properties of asymmetric nuclear matter based on MBPT calculations [27] for six commonly used chiral EFT Hamiltonians with *NN* and 3*N* interactions. The global symmetry energy, i.e., the difference between EOS in the limits of PNM and SNM, as well as its quadratic and quartic contributions have been determined with theoretical

uncertainty estimates. We have calculated the quadratic contribution to the symmetry energy from the usual expansion around SNM and have also employed a nonstandard approach using an expansion for small proton fractions around PNM. The two approaches are in excellent agreement. Furthermore, we have investigated the strength of the nonquadraticities as well as their model dependence. The nonquadratic contribution to the symmetry energy was found to be $0.74^{+0.11}_{-0.08}$ MeV (and $-1.02^{+0.11}_{-0.08}$ MeV for the effective potential part). We have then investigated the leading-order logarithmic term to the symmetry energy, and obtained residuals between our best fit (including quadratic and quartic contributions) and the data to be compatible with zero. In particular, we found that all residuals where flat in the isospin asymmetry δ, indicating no systematic deviation from zero as expected for a logarithmic contribution. However, we also saw that present uncertainties, indicated by the dispersion of the six Hamiltonians of about 1–2 MeV, are too large to precisely determine its strength. For a more recent and complementary approach, see Ref. [81], where the authors have extracted high-order terms using precise modified finite-difference methods.

We analyzed the impact of our results on the determination of the crust-core transition in neutron stars using a simple model in the thermodynamic limit. We found that the crust-core transition density is increased by $\approx$5%, and the associated isospin-asymmetry δ decreased by $\approx$1% when nonquadraticities are included. Hence, these contributions are only small corrections but need to be included for a precise calculation of the core-crust transition properties.

To gauge the full theoretical uncertainties of the nonquadratic contributions to the symmetry energy, future analyses need to explore a wider range of nuclear interactions and additional asymmetric-matter calculations using different many-body approaches and regularization schemes. In particular, this requires the development of improved chiral *NN* and 3*N* interactions up to N^{3}LO [82–84], which will enable order-by-order analyses of the neutron-rich matter EOS with statistically meaningful uncertainty estimates derived from chiral EFT [62,63].

Finally, at densities beyond those explored in this work, heavier baryonic degrees of freedom, such as hyperons, could become relevant. The development and improvement of models that include such degrees of freedom is a crucial task for future work, e.g., along the lines of Refs. [85,86]; see also Refs. [87,88] for recent reviews. Our work provides a framework, e.g., Python codes [28] and Supplemental Material [29] related to our data, for future investigations of the isospin-dependence of nuclear matter.
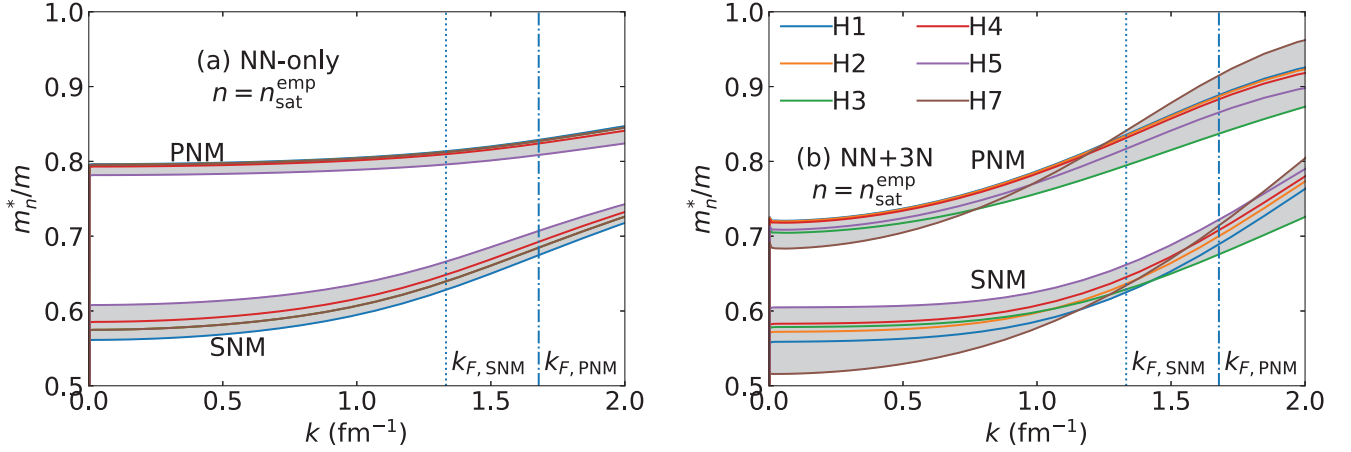
FIG. 10. Same as Fig. 9 but for the neutron effective mass as function of the momentum k.

APPENDIX A: ANALYSIS OF THE SINGLE-PARTICLE SPECTRUM AND THE EFFECTIVE MASS

In Sec. III B we introduced the single-particle energies, the in-medium effective mass, and the Landau effective mass. In this Appendix we quantitatively discuss several of their properties.

First, we consider the single-particle energies calculated from Eq. (7). Figure 9 shows the single-particle energy $\epsilon_n(k)$ in SNM and PNM evaluated at n_{sat}^{emp}. The left (right) panel depicts the NN-only ($NN + 3N$) results, and the vertical lines mark the position of the neutron Fermi momentum in SNM ($k_{F,SNM} = 1.33$ fm^{-3}) and PNM ($k_{F,PNM} = 1.68$ fm^{-3}) associated with the nuclear saturation density, n_{sat}^{emp}. The different curves show the results for the six Hamiltonians H1 to H7 specified in Table I. The spread is larger in SNM (about 15 MeV) compared with PNM (about 5 MeV) because the $3N$ short- and intermediate-range contributions governed by c_D and c_E do not contribute to the PNM EOS for nonlocal regulator functions. As expected, SNM is more attractive than PNM, as a result of the attractive contributions from the $T = 0$ channels, which are absent in PNM.

Let us now move on to the in-medium effective masses calculated using Eq. (9). The effective masses in SNM and PNM are shown in Fig. 10 as functions of the momentum k at a fixed density n_{sat}^{emp}. The effective masses are lower in

SNM compared with PNM, in agreement with BHF calculations [32,89,90]. We find that the inclusion of $3N$ forces leads to several interesting effects on the effective mass: (a) $3N$ forces generate a stronger momentum dependence compared with NN-only calculations, and (b) $3N$ forces have a larger impact on PNM than on SNM. Furthermore, the dispersion among the different Hamiltonians is slightly larger when $3N$ forces are included. From Fig. 10, we find for the Landau mass $m_n^*/m(\delta = 0) = 0.64(2)$ in SNM and $m_n^*/m(\delta = 1) = 0.88(4)$ in PNM when $3N$ forces are included. The difference between the Landau mass in PNM and SNM at saturation density, defined as

$$Dm_{n,sat}^* = m_n^*(n_{sat}, \delta = 1) - m_n^*(n_{sat}, \delta = 0), \quad (A1)$$

is about $Dm_{n,sat}^* = 0.24(5)$ at n_{sat}.

In Fig. 11, we show the Landau mass (left) and its inverse (right) considering NN-only forces (dashed lines) and NN and $3N$ forces (gray bands) in SNM and PNM as a function of the density, n. The difference of the Landau masses in PNM and SNM, $Dm_n^*(n)$, increases with density and is found to be about 0.24 at saturation density, see also Fig. 10. While it is usually found that the Landau mass decreases with density [32,89,90], we find that in PNM the Landau mass first decreases at lower density but increases again for $n > 0.1$ fm^{-3} (except for Hamiltonian H3, which has a higher momentum cutoff applied to the $3N$ forces). This effect is due to the inclusion of $3N$ interactions in the Hamiltonian.

Because many energy density-functional (EDF) approaches approximate the inverse of the Landau mass by a linear function in density [30], we show the inverse Landau mass in the right panel of Figure 11. In contrast to the EDFs approaches, we find that the density dependence of the inverse Landau mass is not linear, and that $3N$ forces enhance the nonlinear behavior.

Finally, we study the splitting of the neutron and proton Landau masses in ANM, defined as

$$\Delta m_{sat}^*(\delta) = m_n^*(n_{sat}, \delta) - m_p^*(n_{sat}, \delta). \quad (A2)$$
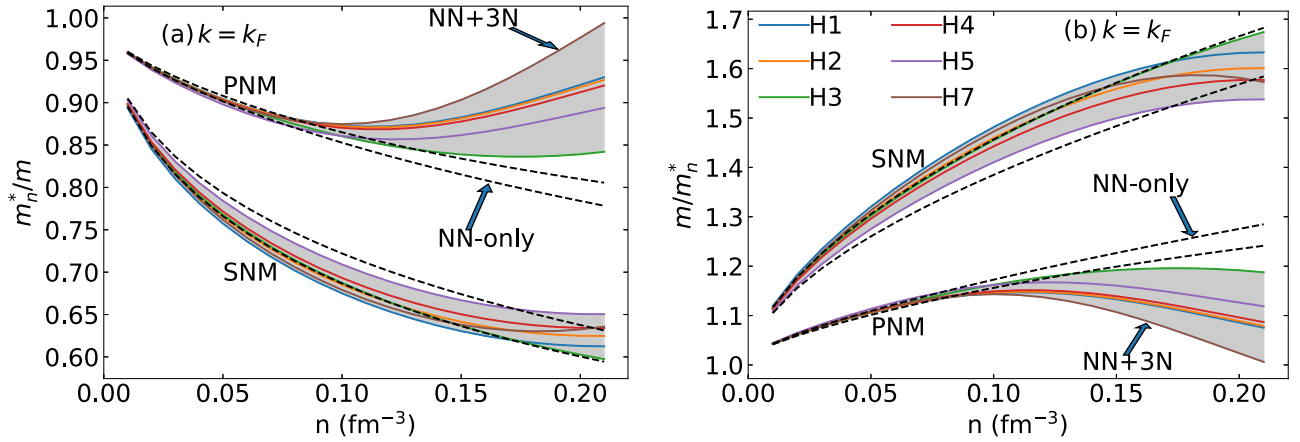
FIG. 11. (a) Landau effective mass and (b) its inverse in SNM and PNM as a function of density. The black-dashed lines represent the upper and lower limits when only *NN* forces are considered, while the gray-shaded regions show the results with 3*N* forces included. The different colors correspond to the six Hamiltonians as labeled in the legend.

In PNM ($\delta = 1$), this splitting can be expressed in terms of the difference Dm^*_{sat}, see Eq. (A1), as

$$\frac{\Delta m^*_{\text{sat}}}{m}(\text{PNM}) \approx \frac{Dm^*_{n,\text{sat}}}{m} + O\left(\left(\frac{\kappa_{\text{sym}} + \kappa_{\text{sym},2}}{1 + \kappa_{\text{sat}} + \kappa_{\text{sat},2}}\right)^2\right). \quad (A3)$$

From our fits estimated in Sec. III B, we can estimate that the neglected terms account for about 5% of the splitting (more precisely, 7% for the linear fit of the effective mass, and 3% for the quadratic fit), which is small considering the present uncertainty of this quantity. The splitting of the Landau mass is, thus, approximately given by the difference of the Landau mass between PNM and SNM. The splitting of the Landau mass obtained here is compatible with the one obtained in the literature for BHF [32,91,92] and Dirac-BHF [89,90] approaches.

APPENDIX B: MAPPING BETWEEN META-MODEL AND EMPIRICAL PARAMETERS

In Sec. IV, the meta-model (MM) was introduced in SNM and PNM. Here, the MM coefficients, $v_{\alpha,1}$ to $v_{\alpha,N}$, are related to the nuclear empirical parameters (NEPs), such as E_{sat}, K_{sat}, E_{sym}, L_{sym}, etc. The NEPs for SNM are defined by the density expansion

$$e_{\text{SNM}}(n) = E_{\text{sat}} + \tfrac{1}{2}K_{\text{sat}}x^2 + \tfrac{1}{6}Q_{\text{sat}}x^3 + \tfrac{1}{24}Z_{\text{sat}}x^4 + \cdots, \quad (B1)$$

whereas the NEPs for PNM are defined by

$$e_{\text{PNM}}(n) = E_{\text{PNM}} + L_{\text{PNM}}x + \tfrac{1}{2}K_{\text{PNM}}x^2 + \tfrac{1}{6}Q_{\text{PNM}}x^3 + \tfrac{1}{24}Z_{\text{PNM}}x^4 + \cdots. \quad (B2)$$

In this Appendix we give the relations between the MM parameters and the NEPs. For the isoscalar parameters controlling the SNM EOS, we have

$$
\begin{aligned}
&v_{\text{SNM},0} = E_{\text{sat}} - t_{\text{SNM}}(1 + \kappa_{\text{sat}} + \kappa_{\text{sat},2}), \quad v_{\text{SNM},1} = -t_{\text{SNM}}(2 + 5\kappa_{\text{sat}} + 8\kappa_{\text{sat},2}), \\
&v_{\text{SNM},2} = K_{\text{sat}} - 2t_{\text{SNM}}(-1 + 5\kappa_{\text{sat}} + 20\kappa_{\text{sat},2}), \quad v_{\text{SNM},3} = Q_{\text{sat}} - 2t_{\text{SNM}}(4 - 5\kappa_{\text{sat}} + 40\kappa_{\text{sat},2}), \\
&v_{\text{SNM},4} = Z_{\text{sat}} - 8t_{\text{SNM}}(-7 + 5\kappa_{\text{sat}} - 10\kappa_{\text{sat},2}),
\end{aligned}
\quad (B3)
$$

while the isovector parameters describing the PNM EOS are

$$
\begin{aligned}
&v_{\text{PNM},0} = E_{\text{PNM}} - 2^{\frac{2}{3}}t_{\text{SNM}}(1 + \kappa_{\text{PNM}} + \kappa_{\text{PNM},2}), \quad v_{\text{PNM},1} = L_{\text{PNM}} - 2^{\frac{2}{3}}t_{\text{SNM}}(2 + 5\kappa_{\text{PNM}} + 8\kappa_{\text{PNM},2}), \\
&v_{\text{PNM},2} = K_{\text{PNM}} - 2^{\frac{5}{3}}t_{\text{SNM}}(-1 + 5\kappa_{\text{PNM}} + 20\kappa_{\text{PNM},2}), \quad v_{\text{PNM},3} = Q_{\text{PNM}} - 2^{\frac{5}{3}}t_{\text{SNM}}(4 - 5\kappa_{\text{PNM}} + 40\kappa_{\text{PNM},2}), \\
&v_{\text{PNM},4} = Z_{\text{PNM}} - 2^{\frac{11}{3}}t_{\text{SNM}}(-7 + 5\kappa_{\text{PNM}} - 10\kappa_{\text{PNM},2}).
\end{aligned}
\quad (B4)
$$

Moreover, In Sec. V B 1, we encountered the quadratic contribution to the symmetry energy as given by the MM, see Eq. (24). The MM parameters appearing in this expression are related to the quadratic symmetry energy NEPs as follows:

$$v_{\text{sym2},0} = E_{\text{sym2}} - \frac{5}{9}t_{\text{SNM}}^{\text{sat}}[1 + \kappa_{\text{sat}} + 3\kappa_{\text{sym}} + \kappa_{\text{sat},2} + 3\kappa_{\text{sym},2}],$$

$$v_{\text{sym2},1} = L_{\text{sym2}} - \frac{5}{9}t_{\text{SNM}}^{\text{sat}}[2 + 5(\kappa_{\text{sat}} + 3\kappa_{\text{sym}}) + 8(\kappa_{\text{sat},2} + 3\kappa_{\text{sym},2})],$$

$$v_{\text{sym2},2} = K_{\text{sym2}} - \frac{10}{9}t_{\text{SNM}}^{\text{sat}}[-1 + 5(\kappa_{\text{sat}} + 3\kappa_{\text{sym}}) + 20(\kappa_{\text{sat},2} + 3\kappa_{\text{sym},2})],$$

$$v_{\text{sym2},3} = Q_{\text{sym2}} - \frac{10}{9}t_{\text{SNM}}^{\text{sat}}[4 - 5(\kappa_{\text{sat}} + 3\kappa_{\text{sym}}) + 40(\kappa_{\text{sat},2} + 3\kappa_{\text{sym},2})],$$

$$v_{\text{sym2},4} = Z_{\text{sym2}} - \frac{40}{9}t_{\text{SNM}}^{\text{sat}}[-7 + 5(\kappa_{\text{sat}} + 3\kappa_{\text{sym}}) - 10(\kappa_{\text{sat},2} + 3\kappa_{\text{sym},2})]. \tag{B5}$$

These relations generalize those in Ref. [17] for a quadratic density-dependent Landau mass.

---

[1] M. Oertel, M. Hempel, T. Klähn, and S. Typel, Rev. Mod. Phys. **89**, 015007 (2017).

[2] G. Fiorella Burgio and A. F. Fantina, Nuclear equation of state for compact stars and supernovae, in *The Physics and Astrophysics of Neutron Stars*, edited by L. Rezzolla, P. Pizzochero, D. I. Jones, N. Rea, and I. Vidaña (Springer International Publishing, Cham, 2018), pp. 255–335.

[3] K. Hebeler, J. Holt, J. Menéndez, and A. Schwenk, Annu. Rev. Nucl. Part. Sci. **65**, 457 (2015).

[4] A. W. Steiner, M. Prakash, J. M. Lattimer, and P. J. Ellis, Phys. Rep. **411**, 325 (2005).

[5] M. Baldo and G. Burgio, Prog. Part. Nucl. Phys. **91**, 203 (2016).

[6] K. Hebeler, J. Lattimer, C. Pethick, and A. Schwenk, Phys. Rev. Lett. **105**, 161102 (2010).

[7] S. Gandolfi, J. Carlson, and S. Reddy, Phys. Rev. C **85**, 032801 (2012).

[8] A. Steiner and S. Gandolfi, Phys. Rev. Lett. **108**, 081102 (2012).

[9] C. Horowitz, E. Brown, Y. Kim, W. Lynch, R. Michaels, A. Ono, J. Piekarewicz, M. Tsang, and H. Wolter, J. Phys. G **41**, 093001 (2014).

[10] N. S. A. C. (NSAC), *2015 Long Range Plan for Nuclear Science*, https://www.aps.org/units/dnp/resources/nuclear.cfm (2015).

[11] S. Abrahamyan *et al.*, Phys. Rev. Lett. **108**, 112502 (2012).

[12] C. J. Horowitz, K. S. Kumar, and R. Michaels, Eur. Phys. J. A **50**, 48 (2014).

[13] X. Roca-Maza, M. Brenna, B. Agrawal, P. Bortignon, G. Colò, L.-G. Cao, N. Paar, and D. Vretenar, Phys. Rev. C **87**, 034301 (2013).

[14] M. Tsang *et al.*, Phys. Rev. C **86**, 015803 (2012).

[15] J. M. Lattimer and A. W. Steiner, Eur. Phys. J. A **50**, 40 (2014).

[16] J. M. Lattimer and Y. Lim, Astrophys. J. **771**, 51 (2013).

[17] J. Margueron, R. Hoffmann Casali, and F. Gulminelli, Phys. Rev. C **97**, 025805 (2018).

[18] M. Dutra, O. Lourenco, J. S. Martins, A. Delfino, J. Stone, and P. Stevenson, Phys. Rev. C **85**, 035201 (2012).

[19] M. Dutra, O. Lourenço, S. Avancini, B. Carlson, A. Delfino, D. Menezes, C. Providência, S. Typel, and J. Stone, Phys. Rev. C **90**, 055203 (2014).

[20] J. E. Lynn, I. Tews, S. Gandolfi, and A. Lovato, Annu. Rev. Nucl. Part. Sci. **69**, 279 (2019).

[21] C. Drischler, J. W. Holt, and C. Wellenhofer, arXiv:2101.01709v1.

[22] A. W. Steiner, Phys. Rev. C **74**, 045808 (2006).

[23] L.-W. Chen, B.-J. Cai, C. M. Ko, B.-A. Li, C. Shen, and J. Xu, Phys. Rev. C **80**, 014322 (2009).

[24] B.-J. Cai and L.-W. Chen, Phys. Rev. C **85**, 024302 (2012).

[25] B.-J. Cai and B.-A. Li, Phys. Rev. C **92**, 011601 (2015).

[26] W. Seif and D. Basu, Phys. Rev. C **89**, 028801 (2014).

[27] C. Drischler, K. Hebeler, and A. Schwenk, Phys. Rev. C **93**, 054314 (2016).

[28] R. Somasundaram, Somasundaram-rahul/nuclear-symmetry-energy (2020).

[29] See Supplemental Material at http://link.aps.org/supplemental/10.1103/PhysRevC.103.045803 for a description of the fit strategy and Python code used to generate the results and figures in this article.

[30] M. Bender, P.-H. Heenen, and P.-G. Reinhard, Rev. Mod. Phys. **75**, 121 (2003).

[31] G. Wlazłowski, J. Holt, S. Moroz, A. Bulgac, and K. Roche, Phys. Rev. Lett. **113**, 182503 (2014).

[32] I. Bombaci and U. Lombardo, Phys. Rev. C **44**, 1892 (1991).

[33] C.-H. Lee, T. Kuo, G. Li, and G. Brown, Phys. Rev. C **57**, 3488 (1998).

[34] T. Frick, H. Muther, A. Rios, A. Polls, and A. Ramos, Phys. Rev. C **71**, 014313 (2005).

[35] I. Vidana, C. Providência, A. Polls, and A. Rios, Phys. Rev. C **80**, 045806 (2009).

[36] N. Kaiser, Phys. Rev. C **91**, 065201 (2015).

[37] C. Wellenhofer, J. W. Holt, and N. Kaiser, Phys. Rev. C **93**, 055802 (2016).

[38] D. R. Entem and R. Machleidt, Phys. Rev. C **68**, 041001 (2003).

[39] K. Hebeler, S. K. Bogner, R. J. Furnstahl, A. Nogga, and A. Schwenk, Phys. Rev. C **83**, 031301 (2011).

[40] M. C. M. Rentmeester, R. G. E. Timmermans, and J. J. de Swart, Phys. Rev. C **67**, 044001 (2003).

[41] J. Simonis, K. Hebeler, J. Holt, J. Menendez, and A. Schwenk, Phys. Rev. C **93**, 011302 (2016).

[42] G. Hagen, A. Ekström, C. Forssén, G. R. Jansen, W. Nazarewicz, T. Papenbrock, K. A. Wendt, S. Bacca, N. Barnea, B. Carlsson, C. Drischler, K. Hebeler, M. Hjorth-Jensen, M. Miorelli, G. Orlandini, A. Schwenk, and J. Simonis, Nat. Phys. **12**, 186 (2016).

[43] R. F. Garcia Ruiz, M. L. Bissell, K. Blaum, A. Ekström, N. Frömmgen, G. Hagen, M. Hammen, K. Hebeler, J. D.

Holt, G. R. Jansen, M. Kowalska, K. Kreim, W. Nazarewicz, R. Neugart, G. Neyens, W. Nörtershäuser, T. Papenbrock, J. Papuga, A. Schwenk, J. Simonis, K. A. Wendt, and D. T. Yordanov, Nat. Phys. **12**, 594 (2016).

[44] G. Hagen, G. R. Jansen, and T. Papenbrock, Phys. Rev. Lett. **117**, 172501 (2016).

[45] J. Simonis, S. R. Stroberg, K. Hebeler, J. D. Holt, and A. Schwenk, Phys. Rev. C **96**, 014303 (2017).

[46] J. Birkhan, M. Miorelli, S. Bacca, S. Bassauer, C. A. Bertulani, G. Hagen, H. Matsubara, P. von Neumann-Cosel, T. Papenbrock, N. Pietralla, V. Y. Ponomarev, A. Richter, A. Schwenk, and A. Tamii, Phys. Rev. Lett. **118**, 252501 (2017).

[47] T. D. Morris, J. Simonis, S. R. Stroberg, C. Stumpf, G. Hagen, J. D. Holt, G. R. Jansen, T. Papenbrock, R. Roth, and A. Schwenk, Phys. Rev. Lett. **120**, 152503 (2018).

[48] S. Stroberg, J. Holt, A. Schwenk, and J. Simonis, Phys. Rev. Lett. **126**, 022501 (2021).

[49] M. Mougeot *et al.*, Phys. Rev. C **102**, 014301 (2020).

[50] S. Kaufmann *et al.*, Phys. Rev. Lett. **124**, 132502 (2020).

[51] A. Akmal, V. R. Pandharipande, and D. G. Ravenhall, Phys. Rev. C **58**, 1804 (1998).

[52] I. Tews, S. Gandolfi, A. Gezerlis, and A. Schwenk, Phys. Rev. C **93**, 024305 (2016).

[53] P. Lepage and C. Gohlke, gplepage/lsqfit: lsqfit version 11.5.1 (2020).

[54] R. B. Wiringa, V. Stoks, and R. Schiavilla, Phys. Rev. C **51**, 38 (1995).

[55] B. Pudliner, V. Pandharipande, J. Carlson, and R. B. Wiringa, Phys. Rev. Lett. **74**, 4396 (1995).

[56] L. Coraggio, A. Covello, A. Gargano, N. Itaco, D. Entem, T. Kuo, and R. Machleidt, Phys. Rev. C **75**, 024311 (2007).

[57] L. Coraggio, J. Holt, N. Itaco, R. Machleidt, and F. Sammarruca, Phys. Rev. C **87**, 014322 (2013).

[58] A. Gezerlis, I. Tews, E. Epelbaum, S. Gandolfi, K. Hebeler, A. Nogga, and A. Schwenk, Phys. Rev. Lett. **111**, 032501 (2013).

[59] A. Gezerlis, I. Tews, E. Epelbaum, M. Freunek, S. Gandolfi, K. Hebeler, A. Nogga, and A. Schwenk, Phys. Rev. C **90**, 054323 (2014).

[60] J. Lynn, I. Tews, J. Carlson, S. Gandolfi, A. Gezerlis, K. Schmidt, and A. Schwenk, Phys. Rev. Lett. **116**, 062501 (2016).

[61] E. Epelbaum, H. Krebs, and U. Meißner, Eur. Phys. J. A **51**, 53 (2015).

[62] C. Drischler, R. J. Furnstahl, J. A. Melendez, and D. R. Phillips, Phys. Rev. Lett. **125**, 202702 (2020).

[63] C. Drischler, J. A. Melendez, R. J. Furnstahl, and D. R. Phillips, Phys. Rev. C **102**, 054315 (2020).

[64] K. Hebeler and A. Schwenk, Phys. Rev. C **82**, 014314 (2010).

[65] J. Jeukenne, A. Lejeune, and C. Mahaux, Phys. Rep. **25**, 83 (1976).

[66] L. Cao, U. Lombardo, C. Shen, and N. Van Giai, Phys. Rev. C **73**, 014313 (2006).

[67] X. Roca-Maza, G. Colo, and H. Sagawa, Phys. Rev. C **86**, 031306 (2012).

[68] B. Fornberg, Math. Comput. **51**, 699 (1988).

[69] J. Margueron and F. Gulminelli, Phys. Rev. C **99**, 025806 (2019).

[70] J. Margueron, R. Hoffmann Casali, and F. Gulminelli, Phys. Rev. C **97**, 025806 (2018).

[71] B.-A. Li, P. G. Krastev, D.-H. Wen, and N.-B. Zhang, Eur. Phys. J. A **55**, 117 (2019).

[72] D. Lonardoni, I. Tews, S. Gandolfi, and J. Carlson, Phys. Rev. Research **2**, 022033 (2020).

[73] I. Tews, T. Krüger, K. Hebeler, and A. Schwenk, Phys. Rev. Lett. **110**, 032504 (2013).

[74] A. Bulgac, M. M. Forbes, S. Jin, R. Navarro Perez, and N. Schunck, Phys. Rev. C **97**, 044313 (2018).

[75] G. Audi, F. G. Kondev, M. Wang, W. Huang, and S. Naimi, Chin. Phys. C **41**, 030001 (2017).

[76] L. Coraggio, J. W. Holt, N. Itaco, R. Machleidt, L. E. Marcucci, and F. Sammarruca, Phys. Rev. C **89**, 044321 (2014).

[77] C. Pethick, D. Ravenhall, and C. Lorenz, Nucl. Phys. A **584**, 675 (1995).

[78] C. Ducoin, J. Margueron, and C. Providência, Europhys. Lett. **91**, 32001 (2010).

[79] C. Ducoin, J. Margueron, C. Providência, and I. Vidana, Phys. Rev. C **83**, 045810 (2011).

[80] P. Lepage, C. Gohlke, and D. Hackett, gplepage/gvar: gvar version 11.7 (2020).

[81] P. Wen and J. W. Holt, arXiv:2012.02163 (2020).

[82] C. Drischler, K. Hebeler, and A. Schwenk, Phys. Rev. Lett. **122**, 042501 (2019).

[83] J. Hoppe, C. Drischler, K. Hebeler, A. Schwenk, and J. Simonis, Phys. Rev. C **100**, 024318 (2019).

[84] T. Hüther, K. Vobig, K. Hebeler, R. Machleidt, and R. Roth, Phys. Lett. B **808**, 135651 (2020).

[85] I. Vidana, A. Polls, A. Ramos, L. Engvik, and M. Hjorth-Jensen, Phys. Rev. C **62**, 035801 (2000).

[86] D. Lonardoni, A. Lovato, S. Gandolfi, and F. Pederiva, Phys. Rev. Lett. **114**, 092301 (2015).

[87] A. Gal, E. V. Hungerford, and D. J. Millener, Rev. Mod. Phys. **88**, 035004 (2016).

[88] L. Tolos and L. Fabbietti, Prog. Part. Nucl. Phys. **112**, 103770 (2020).

[89] K. Hassaneen and H. Muther, Phys. Rev. C **70**, 054308 (2004).

[90] E. van Dalen, C. Fuchs, and A. Faessler, Phys. Rev. Lett. **95**, 022302 (2005).

[91] W. Zuo, I. Bombaci, and U. Lombardo, Phys. Rev. C **60**, 024605 (1999).

[92] W. Zuo, A. Lejeune, U. Lombardo, and J. Mathiot, Nucl. Phys. A **706**, 418 (2002).